

Majorana bound states in germanium Josephson junctions via phase control

Melina Luethi,^{1,*} Henry F. Legg,¹ Katharina Laubscher,² Daniel Loss,¹ and Jelena Klinovaja¹

¹*Department of Physics, University of Basel, Klingelbergstrasse 82, CH-4056 Basel, Switzerland*

²*Condensed Matter Theory Center and Joint Quantum Institute,*

Department of Physics, University of Maryland, College Park, Maryland 20742, USA

(Dated: November 7, 2023)

We consider superconductor-normal-superconductor-normal-superconductor (SNSNS) planar Josephson junctions in hole systems with spin-orbit interaction that is cubic in momentum (CSOI). Using only the superconducting phase difference, we find parameter regimes where junctions of experimentally achievable transparency can enter a topological superconducting phase with Majorana bound states (MBSs) at the junction ends. In planar germanium heterostructures CSOI can be the dominant form of SOI and extremely strong. We show analytically and numerically that, within experimental regimes, our results provide an achievable roadmap for a new MBS platform with low disorder, minimal magnetic fields, and very strong spin-orbit interaction, overcoming many of the key deficiencies that have so far prevented the conclusive observation of MBSs.

I. INTRODUCTION

Majorana bound states (MBSs) [1–7] hold promise for topological quantum computing [8–10]. However, despite enormous effort there has been no conclusive observation of MBSs so far. Key reasons postulated for this are: (1) the level of disorder, which can result in spurious signals that mimic MBSs [11–30]; (2) the small energy scales involved, especially due to the metalization of a semiconductor by a superconductor [31–39]; and (3) many protocols require large magnetic fields [40–53] that are detrimental to superconductors.

Germanium (Ge) has been one of the most used semiconductors since the early days of electronics. The continual interest in Ge [54–67] has resulted in an extremely high quality material [66, 68], with ultralong mean free paths (MFPs) of up to 30 μm [69]. Also, two-dimensional hole gases (2DHG) in Ge have become prominent platforms for quantum information processing [70–78]. Recently, there have also been significant advances in fabricating hybrid superconductor-Ge devices [79–85]. Finally, a most attractive feature of Ge is the large spin-orbit interaction (SOI) [86–90], enabling, e.g., ultrafast qubit operations [66, 91–96]. Most notably, cubic SOI (CSOI) is very strong in Ge 2DHGs [97–99] [100] and results in spin-split Fermi surfaces with large mismatches in velocities, playing a central role in the following.

Despite ultralong MFPs and strong SOI, the small in-plane g factor of Ge ($|g| \lesssim 1.5$) [66, 80, 93, 101–104] is a considerable obstacle to realize MBSs because large Zeeman energies are often required [105, 106]. Only a few proposals have eliminated the need for Zeeman terms, such as time-reversal invariant setups with Kramers pairs of MBSs [107–117]. However, they complicate braiding, thus, systems with broken time-reversal symmetry are preferable. For instance, a π -phase difference across superconductor-normal-superconductor

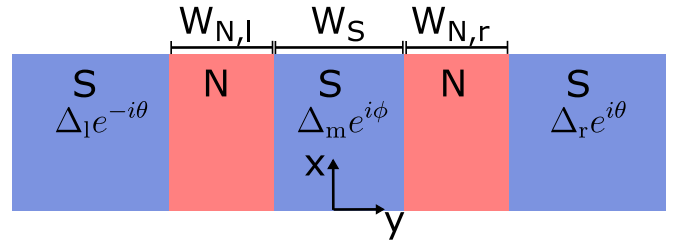


FIG. 1. An SNSNS junction consists of three sections with proximity-induced superconductivity (blue) and two normal conducting sections (red) of width $W_{N,l}$ and $W_{N,r}$. The proximity-induced superconducting gaps are Δ_l , Δ_m , and Δ_r , and the corresponding superconducting phases are $-\theta$, ϕ , and θ . The middle superconductor has a width W_S . The two outer superconductors have widths $W_{S,l}$ and $W_{S,r}$. In the analytical calculations, $W_{S,l}$ and $W_{S,r}$ are infinite, whereas they are finite for the numerical calculations.

(SNS) Josephson junctions requires only a reduced Zeeman energy to produce MBSs [52, 53, 106, 118–120] and enhanced orbital effects in, e.g., topological insulator nanowires enable MBSs without any Zeeman effect [121–123]. Interestingly, utilizing only phase differences in planar SNSNS Josephson junctions (see Fig. 1) it was recently shown that MBSs can exist in electron systems with linear SOI [124]. However, a significant mismatch in velocities of the inner and outer spin-split Fermi surfaces is required, which is difficult to achieve using linear SOI [124].

Here, instead we focus on holes in valence bands described by the Luttinger-Kohn Hamiltonian. We show analytically and numerically that achieving topological superconductivity in SNSNS Josephson junctions with CSOI requires also only phase differences, thereby extending the mechanism proposed for electrons [124] to a different class of systems. Moreover, for such hole systems one finds conditions on the ideal junction geometry that enable large topological regions of phase space, even for reduced junction transparencies. Finally, an in-plane magnetic field provides additional fin-

* melina.luethi@unibas.ch

gerprints of the topological phase. Using realistic parameters for Ge 2DHGs, we argue that recent advances in superconductor-Ge devices enable MBSs to be realized in an experimentally accessible regime. Our results provide a roadmap to achieve topological superconductivity using only weak magnetic fields in a material with ultralong MFPs and large SOI.

The structure of this paper is as follows. We introduce our setup as well as the corresponding Hamiltonian and show results for toy model parameters in Sec. II. In Sec. III, we present results for realistic parameters for Ge, and, furthermore, discuss the effect of an external Zeeman field. We conclude in Sec. IV. In the Appendix, we give more information on the numerical calculations and give derivations of equations shown in the main text.

II. SNSNS JOSEPHSON JUNCTIONS WITH CSOI

Materials with CSOI have large differences in velocities at the inner and outer Fermi surfaces; see Fig. 2(a). In particular, a 2DHG in Ge confined to the crystallographic xy plane [97, 125] has large and dominant CSOI of Rashba type with negligible linear SOI [126]. Anticipating superconductivity, we introduce the Nambu basis $\Psi(x, y) = (\psi_\uparrow(x, y), \psi_\downarrow(x, y), \psi_\uparrow^\dagger(x, y), \psi_\downarrow^\dagger(x, y))^T$, where $\psi_s^\dagger(x, y)$ creates a particle at position (x, y) with spin s . In this basis, the effective Hamiltonian of a Ge 2DHG, derived using the Luttinger-Kohn formalism, is [97–99]

$$\begin{aligned} \mathcal{H}_{\text{eff}} = & \left[-\frac{\hbar^2}{2m^*} (\partial_x^2 + \partial_y^2) - \mu \right] \tau_z + 2i\alpha \left[\partial_y (\partial_y^2 - 3\partial_x^2) \sigma_x \right. \\ & \left. + \partial_x (\partial_x^2 - 3\partial_y^2) \sigma_y \tau_z \right] - 2i\alpha_a (\partial_x^2 + \partial_y^2) (\partial_y \sigma_x + \partial_x \sigma_y \tau_z), \end{aligned} \quad (1)$$

where m^* is the effective mass, σ_i (τ_i) are the Pauli matrices acting in spin (particle-hole) space, and α and α_a are the strengths of the CSOI. The term α_a comes from anisotropic corrections and for Ge $\alpha_a \ll \alpha$ [97]. As discussed in Ref. [106], throughout we also introduce a quartic term $\mathcal{H}_4 = \beta(\partial_x^4 + \partial_y^4 + 2\partial_x^2\partial_y^2)\tau_z$ to avoid spurious additional Fermi surfaces in discretized numerical calculations. The exact size of β does not affect our results. The energy spectrum of the full normal state Hamiltonian $\mathcal{H} = \mathcal{H}_{\text{eff}} + \mathcal{H}_4$ in momentum space has two spin-split Fermi surfaces, labeled by $j = 1$ ($j = 2$) for the inner (outer) Fermi surface. The corresponding Fermi velocities are different; see inset of Fig. 2(a). These velocities may be tuned by varying the SOI strength or the chemical potential μ .

The SNSNS junction comprises three sections that are proximitized by superconductors and two normal sections between them; see Fig. 1. The Hamiltonian for the proximity-induced superconducting potential is

$$\mathcal{H}_{\text{SC}} = i\sigma_y [\Delta^*(y)\tau_+ - \Delta(y)\tau_-] / 2 \quad (2)$$

with $\tau_\pm = \tau_x \pm i\tau_y$ and

$$\Delta(y) = \begin{cases} \Delta_l e^{-i\theta} & \text{if } y < -W_{N,l} - \frac{W_S}{2}, \\ \Delta_m e^{i\phi} & \text{if } -\frac{W_S}{2} \leq y < \frac{W_S}{2}, \\ \Delta_r e^{i\theta} & \text{if } W_{N,r} + \frac{W_S}{2} \leq y, \\ 0 & \text{otherwise,} \end{cases} \quad (3)$$

where $W_{N,l}$ ($W_{N,r}$) is the width of the left (right) normal section, and W_S the width of the middle superconductor.

While a Zeeman field is not required to enter the topological phase, we will demonstrate later that it can be beneficial and provide additional features to distinguish MBSs from trivial bound states. The Hamiltonian for a magnetic field of strength B applied in x direction along the junction is $\mathcal{H}_Z = \Delta_Z(y)\sigma_x\tau_z$, where for simplicity we use

$$\Delta_Z(y) = \begin{cases} \Delta_Z & \text{if } -W_{N,l} - \frac{W_S}{2} \leq y < -\frac{W_S}{2}, \\ & \text{or } \frac{W_S}{2} \leq y < W_{N,r} + \frac{W_S}{2}, \\ 0 & \text{otherwise,} \end{cases} \quad (4)$$

and $\Delta_Z = g\mu_B B$ with g the g factor of the material and μ_B the Bohr magneton. The induced superconducting gap is reduced as a magnetic field is applied, however, we focus on small magnetic fields and therefore neglect the reduction of the induced gap. To take into account that the junction does not have perfect transparency, we introduce a potential barrier $\mathcal{H}_b = \mu_b(y)\tau_z$, where

$$\mu_b(y) = \begin{cases} \mu_b & \text{if } y_b - \frac{W_b}{2} \leq y < y_b + \frac{W_b}{2}, \\ 0 & \text{otherwise,} \end{cases} \quad (5)$$

where $y_b \in \{-W_{N,l} - \frac{W_S}{2}, -\frac{W_S}{2}, \frac{W_S}{2}, W_{N,r} + \frac{W_S}{2}\}$ and W_b is the width of the barrier. The full Hamiltonian of the system is

$$\mathcal{H} = \mathcal{H}_{\text{eff}} + \mathcal{H}_4 + \mathcal{H}_{\text{SC}} + \mathcal{H}_Z + \mathcal{H}_b. \quad (6)$$

For now, neglecting the potential barrier and, for simplicity, assuming that $W_{N,l} = W_{N,r} \equiv W_N$ and that the Fermi velocities in both normal conducting sections are equal, the phase transition curves are given by

$$\cos\left(\theta + \frac{2\Delta_Z W_N (-1)^j}{v_j^N}\right) + \tanh\left(\frac{W_S \Delta_m}{v_j^{S,m}}\right) \cos(\phi) = 0, \quad (7)$$

where $j = 1$ ($j = 2$) indicates the inner (outer) Fermi surface and v_j^N ($v_j^{S,m}$) are the Fermi velocities of the corresponding Fermi surface in the normal conducting (middle superconducting) section. The topological phase is between the two curves defined by $j = 1$ and $j = 2$. In Appendix A, we consider a more general case of $W_{N,l} \neq W_{N,r}$ as well as of different Fermi velocities in each section. A larger CSOI strength α results in a larger difference of velocities at the Fermi level, which increases the topological region of phase space; see Fig. 2(a).

To study the system numerically, the full Hamiltonian \mathcal{H} is discretized. We utilize two different geometries: In

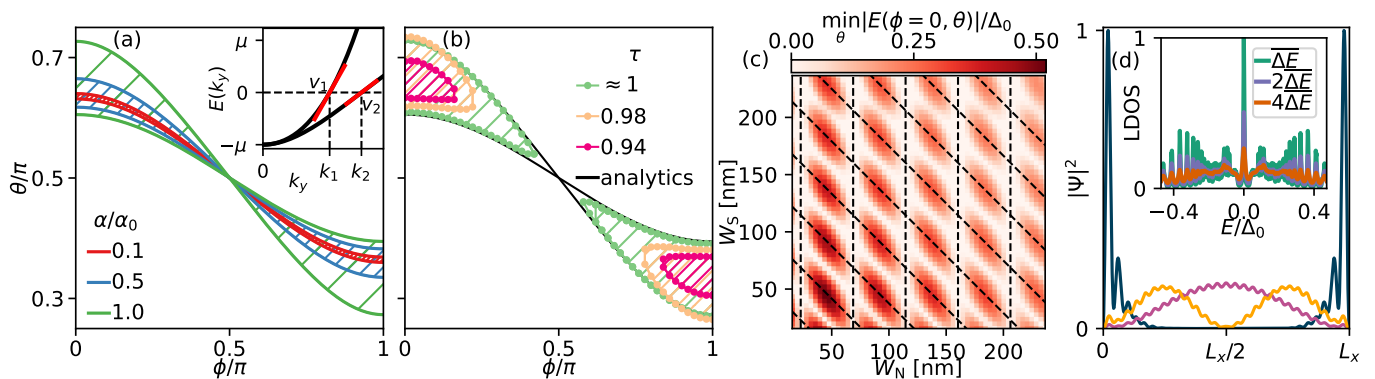


FIG. 2. (a) Analytically calculated phase diagram [see Eq. (7)] for different CSOI strengths α , compared to $\alpha_0 = 1600 \text{ meV nm}^3$ [106], which is also the CSOI strength used in panels (b)-(d). The topological phase is indicated by the hatched region. The two different Fermi velocities v_1 and v_2 , and Fermi momenta k_1 and k_2 are shown in the inset. The larger α is, the more v_1 and v_2 differ and therefore the larger is the topological phase. (b) Numerically calculated bulk gap closing points, i.e., the points where $E(k_x = 0) = 0$, for different transparencies τ controlled via the tunneling barrier height μ_b . The topological phase is indicated by the hatched region. An imperfect transparency reduces the size of the topological phase region, therefore highly transparent junctions are favorable. We set $\mu_b = 0$ for $\tau \approx 1$, $\mu_b = 1.3 \text{ meV}$ for $\tau = 0.98$, and $\mu_b = 6.0 \text{ meV}$ for $\tau = 0.94$. (c) Minimum energy $\min_\theta |E(k_x = 0, \phi = 0, \theta)|$ in the semi-infinite geometry at $k_x = 0$ and $\phi = 0$. The tunneling barrier is fixed to 2 meV. The dashed lines indicate the ideal junction geometry conditions of Eq. (8), for which a topological phase exists even at a low transparency. (d) Profile of the probability distribution $|\Psi|^2$ (arbitrary units) of the lowest energy state, i.e., the MBS (dark blue, $E/\Delta_m = 7.4 \cdot 10^{-6}$), the first excited state (yellow, $E/\Delta_m = 0.035$), and the third excited state (pink, $E/\Delta_m = 0.037$), going through the left normal section in the finite geometry. The second excited state is not shown because it looks similar to the first excited state. In contrast to all other calculations shown, the junction here has a finite length $L_x = 2 \mu\text{m}$ in x direction. The inset shows the local density of states (LDOS) integrated over a small section at the junction end for three different energy broadening coefficients ($\overline{\Delta E}$, $2\overline{\Delta E}$ and $4\overline{\Delta E}$, where $\overline{\Delta E}$ is the average level spacing), see Appendix E. Although there are several in-gap states, the MBSs are well discernible as zero-energy peaks because the Andreev bound states are delocalized over the full length of the normal section. The parameters, taken from Ref. [106], are $\hbar^2/2m^* = 580 \text{ meV nm}^2$, $\alpha_a = 0$, $\beta = 4600 \text{ meV nm}^4$, $\mu = 2.4 \text{ meV}$, $\Delta_0 = 0.26 \text{ meV}$ in panels (a)-(c), and $\Delta_0 = 0.8 \text{ meV}$ in panel (d). The junction size in panels (a) and (b) is $W_N = 28 \text{ nm}$ and $W_S = 130 \text{ nm}$. In panel (d) $W_N = 20 \text{ nm}$ and $W_S = 68 \text{ nm}$. These parameters reveal the qualitative behavior of the system and are easily tractable numerically. We study realistic parameters later; see Fig. 3. We give all parameters rounded to two significant digits. All parameter values used for the numerical calculations are given in Appendix B3.

the finite geometry, a finite extent in both x and y direction is assumed. In the semi-infinite geometry, it is assumed that the junction has a finite extent along the y direction, but is infinitely extended along the x direction, in this case, the momentum k_x along the x axis is a good quantum number. The discretized Hamiltonians for both cases are given in Appendix B. In the following, for simplicity, we also assume a constant pairing potential, $\Delta_l = \Delta_m = \Delta_r = \Delta_0$, in the superconducting sections.

The topological phase transition is of class D [124], which is characterized by a closing of the bulk gap at momentum $k_x = 0$ [53]. This allows us to calculate the phase diagram numerically; see Fig. 2(b). Imperfect transparency has a noticeable effect on the phase diagram, reducing the topological region of phase space. To estimate the transparency, we calculate the current-phase relation, see Appendix C. An imperfect transparency is caused by normal reflection at the SN interfaces [53], which is neglected in the analytical derivation. However, assuming $W_{N,1} = W_{N,r} \equiv W_N$ and Fermi momenta k_1 (k_2) for the inner (outer) Fermi surfaces within the junction, see inset of Fig. 2(a), values for W_N and W_S exist for which the effects of scattering are minimized (see Ap-

pendix D):

$$W_N = \frac{(2n+1)\pi}{k_1+k_2}, \quad W_S + W_N = \frac{2m\pi}{k_1+k_2}, \quad n, m \in \mathbb{Z}. \quad (8)$$

We will refer to the conditions in Eq. (8) as the ideal junction geometry. At $k_x = 0$ and $\phi = 0$ – the region where the topological phase disappears last with decreasing transparency – the minimum energy for varying θ , $\min_\theta |E(k_x = 0, \phi = 0, \theta)|$, determines whether a topological phase can still exist at a certain value of the tunneling barrier μ_b . If the minimum is zero, a topological phase still exists. Therefore, at sufficiently high tunneling barriers, only systems with W_S and W_N close to the ideal junction geometry can still be topological; see Fig. 2(c). In an experiment, however, W_S and W_N are fixed after fabrication. In this case, the chemical potential can be tuned, which changes the Fermi momenta and therefore brings the system into a favorable configuration, where either one of the ideal junction geometry conditions is fulfilled, see Appendix D. Systems in which both conditions of the ideal junction geometry are fulfilled are particularly favorable, as they allow for topological phases with particularly low transparencies. The deviation between

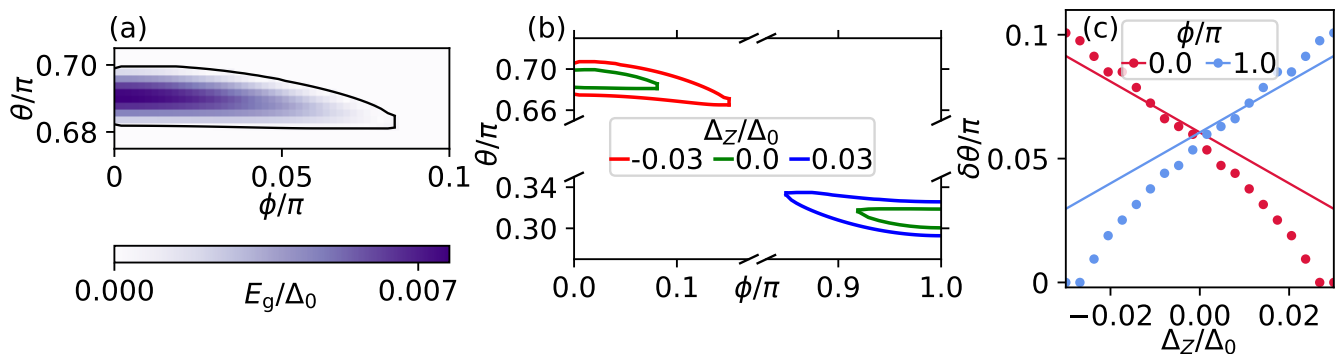


FIG. 3. (a) Phase diagram for realistic Ge parameters, without Zeeman field. The black line indicates the topological phase transition. In the topological phase (purple area), we calculate the topological gap E_g , which is defined in the semi-infinite geometry as $E_g = \min_{k_x} |E(k_x)|$. For realistic parameters we find that there exists a finite topological region of phase space. (b) Phase diagram for realistic Ge parameters, with a small external Zeeman field Δ_Z in x direction. Without any Zeeman field, the phase diagram is symmetric under a π -rotation about $(\pi/2, \pi/2)$. Adding a Zeeman term breaks this symmetry, but increases the total area of the topological phase space. (c) The distance $\delta\theta$ between the two phase transition curves at different values of ϕ as a function of the Zeeman field Δ_Z . The dots (lines) represent numerical (analytical) results. Panels (b) and (c) demonstrate that the magnetic field breaks the rotational symmetry of phase space, giving an additional tool to distinguish MBSs from trivial states. For Ge, we use the following parameters [106, 127]: $\hbar^2/2m^* = 620 \text{ meV nm}^2$, $\alpha = 190 \text{ meV nm}^3$, $\alpha_a = 23 \text{ meV nm}^3$, $\mu = 7.4 \text{ meV}$, $W_S = 170 \text{ nm}$, $W_{N,l} = W_{N,r} = 72 \text{ nm}$, $\beta = 74 \text{ meV nm}^4$, and $\mu_b = 12 \text{ meV}$ such that the transparency of the junction is $\tau = 0.96$ (see Appendix C for more information about the transparency calculation). We set the induced superconducting gap in germanium to $\Delta_m = 0.49 \text{ meV}$, which is from Ref. [84], where germanium is proximitized by superconducting aluminum and niobium. All parameters are rounded to two significant digits. All parameter values used for the numerical calculations are given in Appendix B 3.

the numerical and analytical ideal junction geometry in Fig. 2(c) is further discussed in Appendix D.

Although the topological gap of an SNSNS junction might not be large, as is also the case in SNS junctions [53, 106], MBSs are still clearly discernible as zero-energy peaks in the LDOS at the junction ends because the low-energy Andreev bound states in planar Josephson junctions are delocalized over the full length of the normal section; see Fig. 2(d) and Appendix F.

III. REALISTIC PARAMETERS FOR GERMANIUM

So far, using toy model parameters, we have demonstrated that an SNSNS junction based on a material with CSOI is a good candidate to host MBSs and we have shown the qualitative behavior of such systems. It was shown in Ref. [85] that fabricating Ge SNS junctions with transparencies up to 0.96 is possible. Using realistic parameters, we find a finite topological region of phase space, as shown in Fig. 3(a). We note that the topological gap in this realistic case is rather small, however, we discussed in Fig. 2(d) that the first few excited states of planar Josephson junctions are spatially more extended than the MBSs. Therefore, a clear zero-energy peak in the local density of states at the junction ends is to be expected.

A. Including a Zeeman field

Given the small g factor in Ge, a considerable advantage of a planar SNSNS junction compared to SNS junctions is that no Zeeman field is required to enter the topological phase. However, applying a magnetic field parallel to the junction does not destroy the topological region of phase space. In fact, a parallel magnetic field increases the total area of the topological phase region, see Fig. 3(b) and Appendix A 1. A magnetic field further breaks inversion symmetry which gives an additional tool to distinguish MBSs from trivial states; see Fig. 3(c). Here, we plot the distance $\delta\theta$ between the two phase transition curves at a fixed ϕ . Although the total topological area of phase space increases with a magnetic field, depending on ϕ and the sign of Δ_Z , the difference $\delta\theta$ may increase or decrease. This is important because the antisymmetric behavior of the topological phase in a magnetic field provides an extra signature by which we can distinguish topological from trivial features. For instance, a zero-bias peak with a topological origin would be expected to be less robust against, e.g., changes in the superconducting phase difference θ for the magnetic field in one direction compared to the opposite direction, because $\delta\theta(\Delta_Z) \neq \delta\theta(-\Delta_Z)$.

IV. CONCLUSION

We demonstrated that the dominant cubic SOI in a Ge 2DHG is ideal for hosting MBSs in SNSNS junctions. The SNSNS junction enters the topological phase without any Zeeman term, which eliminates the large magnetic fields that enable many trivial effects to mimic MBSs and provides a route to topological superconductivity in Ge despite the small g factor. Further, we show that an imperfect transparency is detrimental for the topological phase. However, we derive conditions on the ideal junction geometry for which a topological phase exists for experimentally achievable transparencies and parameters. The ideal junction geometry can be approached, e.g., by gating the junction. Finally, although not necessary for MBSs within our setup, we also show that a Zeeman field increases the topological phase region and provides an additional tool to distinguish MBSs from trivial states.

ACKNOWLEDGMENTS

We thank Omri Lesser and Yuval Oreg for useful conversations. This work was supported by the Swiss National Science Foundation and NCCR SPIN (Grant No. 51NF40-180604). This project received funding from the European Union's Horizon 2020 research and innovation program (ERC Starting Grant, Grant Agreement No. 757725). H.F.L acknowledges support by the Georg H. Endress Foundation. K. L. acknowledges support by the Laboratory for Physical Sciences through the Condensed Matter Theory Center.

Appendix A: Derivation of phase diagram with a Zeeman field

In this Appendix, the analytical expression for the topological phase transition curve [see Eq. (7)] is derived. The derivation generalizes the one of Ref. [124] by including also a magnetic field in x direction. Perfect transparency of the junction is assumed. Later, in Appendix D, we will consider the impact of imperfect transparency and demonstrate the existence of an ideal junction geometry.

Since a topological phase transition is characterized by a bulk gap closing at $k_x = 0$, we set $k_x = 0$ in the momentum space version of Eq. (1) and linearize the spectrum, giving four branches; see Fig. 4. We assume that the Zeeman term is only a perturbation to the spectrum and therefore linearize without the Zeeman term. For $k_x = 0$, the Hamiltonian commutes with σ_x and therefore the spin along the x direction S_x is a good quantum number. Based on the direction of the Fermi velocity and the spin of the branch, we label the slow-varying fermionic fields as $L_{\pm}(k_y)$ and $R_{\pm}(k_y)$ (L refers to left-movers, R to right-movers, and the \pm labels the spin eigenvalues)

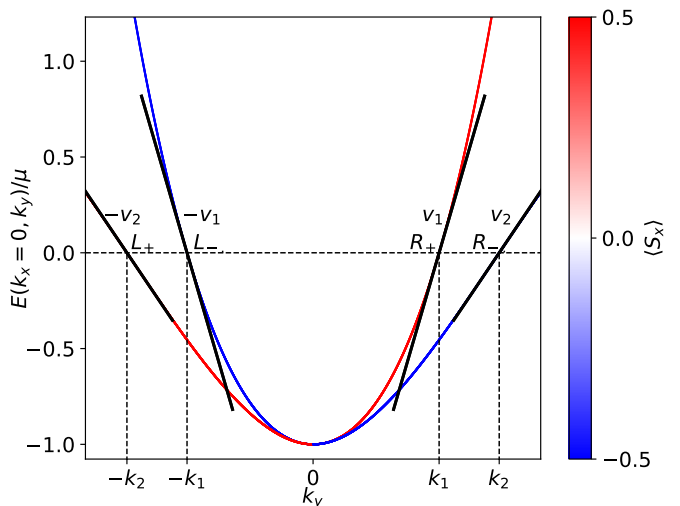


FIG. 4. Spectrum of the effective Hamiltonian $\mathcal{H}_{\text{eff}} + \mathcal{H}_4$ defined in the main text for $k_x = 0$ with the linearized functions L_{\pm} (left movers) and R_{\pm} (right movers), the Fermi momenta $\pm k_{1,2}$, and the Fermi velocities $\pm v_{1,2}$. The color indicates the expectation value $\langle S_x \rangle$ of the spin in x direction.

and their corresponding Fermi momenta and Fermi velocities as k_j and v_j , $j = 1, 2$, respectively. The linearized spectrum is thus given by [7]

$$H_{\text{kin}} = -v_2 L_+^\dagger \hat{k}_y L_+ - v_1 L_-^\dagger \hat{k}_y L_- + v_1 R_+^\dagger \hat{k}_y R_+ + v_2 R_-^\dagger \hat{k}_y R_-, \quad (\text{A1})$$

where \hat{k}_y is the momentum operator in y direction and we assume $v_j > 0$ and $k_j > 0$. Since σ_x commutes with the Hamiltonian, we will consider only states ψ_{\pm} that are simultaneous eigenstates of σ_x and the Hamiltonian, the index \pm indicating their eigenvalue with respect to σ_x . Using the linearized ansatz, ψ_{\pm} can be written as [7, 128]

$$\begin{aligned} \psi_+(y) &= e^{-ik_2 y} L_+(y) + e^{ik_1 y} R_+(y), \\ \psi_-(y) &= e^{-ik_1 y} L_-(y) + e^{ik_2 y} R_-(y). \end{aligned} \quad (\text{A2})$$

To get the linearized version of the superconducting and the Zeeman term, we use

$$\psi_{\uparrow} = \frac{1}{\sqrt{2}}(\psi_+ + \psi_-), \quad \psi_{\downarrow} = \frac{1}{\sqrt{2}}(\psi_+ - \psi_-), \quad (\text{A3})$$

where $\psi_{\uparrow/\downarrow}$ are spin eigenstates of σ_z . Assuming a superconducting term with pairing potential Δ and phase γ , the superconducting part becomes

$$\begin{aligned} H_{\text{SC}} &= \frac{\Delta}{2} \left\{ [\psi_{\uparrow} \psi_{\downarrow} - \psi_{\downarrow} \psi_{\uparrow}] e^{i\gamma} + [\psi_{\downarrow}^\dagger \psi_{\uparrow}^\dagger - \psi_{\uparrow}^\dagger \psi_{\downarrow}^\dagger] e^{-i\gamma} \right\} \\ &= \frac{\Delta}{2} \left\{ [L_- R_+ - R_+ L_- + R_- L_+ - L_+ R_-] e^{i\gamma} \right. \\ &\quad \left. + [R_+^\dagger L_-^\dagger - L_-^\dagger R_+^\dagger + L_+^\dagger R_-^\dagger - R_-^\dagger L_+^\dagger] e^{-i\gamma} \right\} \\ &\quad + \text{oscillating terms}, \end{aligned} \quad (\text{A4})$$

while the Zeeman term with Zeeman field Δ_Z reads

$$\begin{aligned} H_Z &= \Delta_Z \left[\psi_{\uparrow}^{\dagger} \psi_{\downarrow} + \psi_{\downarrow}^{\dagger} \psi_{\uparrow} \right] \\ &= \Delta_Z \left[L_{+}^{\dagger} L_{+} + R_{+}^{\dagger} R_{+} - L_{-}^{\dagger} L_{-} - R_{-}^{\dagger} R_{-} \right] \\ &\quad + \text{oscillating terms.} \end{aligned} \quad (\text{A5})$$

In the following, we neglect the fast oscillating terms [7]. In the basis $c(k_y) = (R_{+}, L_{-}^{\dagger}, L_{-}, R_{+}^{\dagger}, R_{-}, L_{+}^{\dagger}, L_{+}, R_{-}^{\dagger})^T$, the full Hamiltonian $H = H_{\text{kin}} + H_{\text{SC}} + H_Z$ is block-diagonal:

$$H = \begin{pmatrix} \mathcal{H}(v_1 k_y) & 0 & 0 & 0 \\ 0 & -\mathcal{H}(v_1 k_y) & 0 & 0 \\ 0 & 0 & -\mathcal{H}(-v_2 k_y) & 0 \\ 0 & 0 & 0 & \mathcal{H}(-v_2 k_y) \end{pmatrix}, \quad (\text{A6})$$

$$\mathcal{H}(vk) = \begin{pmatrix} vk + \Delta_Z & \Delta e^{-i\gamma} \\ \Delta e^{i\gamma} & -vk + \Delta_Z \end{pmatrix}. \quad (\text{A7})$$

Since the Hamiltonian is block-diagonal, one can calculate the wave function for each block independently. Depending on the block, the Fermi velocity is either positive or negative. Thus, we assume a general Hamiltonian $\mathcal{H}(vk)$ as defined in Eq. (A7), where the Fermi velocity $v = \pm v_1, \pm v_2$ can both be positive or negative.

First, consider the superconducting region: We assume that there is no Zeeman term in this region, therefore giving the Hamiltonian

$$\mathcal{H}(vk) = \begin{pmatrix} vk & \Delta e^{-i\gamma} \\ \Delta e^{i\gamma} & -vk \end{pmatrix}. \quad (\text{A8})$$

As such, the energy in this region is given by

$$E = \pm \sqrt{k^2 v^2 + \Delta^2}. \quad (\text{A9})$$

Since we are interested in a closing of the bulk gap we set $E = 0$, giving

$$k = \pm i \frac{\Delta}{v} \quad (\text{A10})$$

The corresponding eigenvector is

$$\omega_{\pm}^{\text{S}} = \begin{pmatrix} \pm i e^{-i\gamma} \\ 1 \end{pmatrix}. \quad (\text{A11})$$

In the normal section, we assume a Zeeman energy Δ_Z and thus the Hamiltonian is

$$\mathcal{H}(vk) = \begin{pmatrix} vk + \Delta_Z & 0 \\ 0 & -vk + \Delta_Z \end{pmatrix}. \quad (\text{A12})$$

The energy and eigenfunctions in this region are:

$$E = \pm vk + \Delta_Z \stackrel{!}{=} 0 \Rightarrow k = \pm \frac{\Delta_Z}{v} \quad (\text{A13})$$

and the eigenvectors are

$$\omega_{+}^{\text{N}} = \begin{pmatrix} 0 \\ 1 \end{pmatrix}, \quad \omega_{-}^{\text{N}} = \begin{pmatrix} 1 \\ 0 \end{pmatrix}. \quad (\text{A14})$$

We now make an ansatz for the wave function in each section of the SNSNS junction separately. We assume that the junction has perfect transparency, therefore there is no normal scattering. Thus, each block of the Hamiltonian defined in Eq. (A6) can be considered separately. Generally, the chemical potential may be different in each section. Thus, we assume different Fermi momenta and velocities in each section, i.e., $k^{\text{S},1}$ and $v^{\text{S},1}$, $k^{\text{S},\text{m}}$ and $v^{\text{S},\text{m}}$, and $k^{\text{S},\text{r}}$ and $v^{\text{S},\text{r}}$ in the left, middle, and right superconductors, respectively, and $k^{\text{N},1}$ and $v^{\text{N},1}$ ($k^{\text{N},\text{r}}$ and $v^{\text{N},\text{r}}$) in the left (right) normal section. The widths of the normal sections are $W_{\text{N},1}$ and $W_{\text{N},\text{r}}$, respectively. The left and right superconducting sections are assumed to be infinitely extended, the middle superconducting section has a width W_{S} . The induced superconducting gaps (superconducting phases) are Δ_1 ($-\theta$) in the left, Δ_{m} (ϕ) in the center, and Δ_{r} (θ) in the right superconducting sections; see Fig. 1. We choose the coordinate system such that the interface between the left superconductor and the left normal section is at $y = 0$. Note that this convention is different from the convention used in Fig. 1, where $y = 0$ is in the center of the middle superconductor.

Because the left superconductor is infinitely extended, only wave functions that are decaying for $y \rightarrow -\infty$ are valid. Therefore, the wave function in the left superconducting region contains either only ω_{+}^{S} or only ω_{-}^{S} , depending on the sign of $v^{\text{S},1}$:

$$\Psi_{\text{S},1}(y) = e^{y\Delta_1/|v^{\text{S},1}|} \begin{pmatrix} -i \operatorname{sgn}(v^{\text{S},1}) e^{i\theta} \\ 1 \end{pmatrix}. \quad (\text{A15})$$

We emphasize that one gets the same type of the wave function for each of the four blocks defined by the Hamiltonian of Eq. (A6) separately. However, the basis in which Eq. (A15) is defined depends on the block under consideration. Following the same arguments, the wave function in the right superconducting section must be exponentially decaying for $y \rightarrow \infty$ and is therefore given by:

$$\Psi_{\text{S},\text{r}}(y) = A_{\text{S},\text{r}} e^{-y\Delta_{\text{r}}/|v^{\text{S},\text{r}}|} \begin{pmatrix} i \operatorname{sgn}(v^{\text{S},\text{r}}) e^{-i\theta} \\ 1 \end{pmatrix}. \quad (\text{A16})$$

In the middle superconducting region, the ansatz for the wave function is:

$$\begin{aligned} \Psi_{\text{S},\text{m}}(y) &= A_{\text{S},\text{m}} e^{-y\Delta_{\text{m}}/v^{\text{S},\text{m}}} \begin{pmatrix} i e^{-i\phi} \\ 1 \end{pmatrix} \\ &\quad + B_{\text{S},\text{m}} e^{y\Delta_{\text{m}}/v^{\text{S},\text{m}}} \begin{pmatrix} -i e^{-i\phi} \\ 1 \end{pmatrix}. \end{aligned} \quad (\text{A17})$$

The ansatz for the wave function $\Psi_{\text{N},1}$ ($\Psi_{\text{N},\text{r}}$) in the left (right) normal region is

$$\begin{aligned} \Psi_{\text{N},1/\text{r}} &= A_{\text{N},1/\text{r}} e^{iy\Delta_Z/v^{\text{N},1/\text{r}}} \begin{pmatrix} 0 \\ 1 \end{pmatrix} \\ &\quad + B_{\text{N},1/\text{r}} e^{-iy\Delta_Z/v^{\text{N},1/\text{r}}} \begin{pmatrix} 1 \\ 0 \end{pmatrix}. \end{aligned} \quad (\text{A18})$$

Next, all wave function parameters are determined by matching boundary conditions. As mentioned before, we assume perfect transparency and therefore the matching process can be done for each block defined by the Hamiltonian of Eq. (A6) separately as there is no back-

scattering in this approach. Furthermore, since we consider a linearized spectrum, matching only the wave functions is sufficient, it is not required to match their first derivative. At the first interface we get:

$$\Psi_{S,l}(0) = \Psi_{N,l}(0) \Leftrightarrow \begin{pmatrix} -i \operatorname{sgn}(v^{S,l}) e^{i\theta} \\ 1 \end{pmatrix} = T_1 \begin{pmatrix} A_{N,l} \\ B_{N,l} \end{pmatrix} \Leftrightarrow \begin{pmatrix} A_{N,l} \\ B_{N,l} \end{pmatrix} = T_1 \begin{pmatrix} -i \operatorname{sgn}(v^{S,l}) e^{i\theta} \\ 1 \end{pmatrix}, \quad (\text{A19})$$

$$T_1 = \begin{pmatrix} 0 & 1 \\ 1 & 0 \end{pmatrix}, \quad (\text{A20})$$

using $T_1^{-1} = T_1$.

The second interface is at $y = W_{N,l}$, between the left normal section and the middle superconducting region. We require:

$$\begin{aligned} \Psi_{N,l}(W_{N,l}) &= \Psi_{S,m}(W_{N,l}) \Leftrightarrow T_1 D_N(W_{N,l}, v^{N,l}) \begin{pmatrix} A_{N,l} \\ B_{N,l} \end{pmatrix} = T_2 D_S(W_{N,l}, \Delta_m, v^{S,m}) \begin{pmatrix} A_{S,m} \\ B_{S,m} \end{pmatrix} \\ &\Leftrightarrow \begin{pmatrix} A_{S,m} \\ B_{S,m} \end{pmatrix} = D_S(-W_{N,l}, \Delta_m, v^{S,m}) T_2^{-1} T_1 D_N(W_{N,l}, v^{N,l}) \begin{pmatrix} A_{N,l} \\ B_{N,l} \end{pmatrix}, \end{aligned} \quad (\text{A21})$$

where we define

$$T_2 = \begin{pmatrix} ie^{-i\phi} & -ie^{-i\phi} \\ 1 & 1 \end{pmatrix}, \quad (\text{A22})$$

$$D_N(W, v) = \begin{pmatrix} e^{iW\Delta_z/v} & 0 \\ 0 & e^{-iW\Delta_z/v} \end{pmatrix}, \quad (\text{A23})$$

$$D_S(W, \Delta, v) = \begin{pmatrix} e^{-W\Delta/v} & 0 \\ 0 & e^{W\Delta/v} \end{pmatrix}, \quad (\text{A24})$$

and using $D_N(W, v)^{-1} = D_N(-W, v)$ and $D_S(W, \Delta, v)^{-1} = D_S(-W, \Delta, v)$.

The third intersection at $y = W_{N,l} + W_S$ is between the middle superconducting region and the right normal section:

$$\begin{aligned} \Psi_{S,m}(W_{N,l} + W_S) &= \Psi_{N,r}(W_{N,l} + W_S) \Leftrightarrow T_2 D_S(W_{N,l} + W_S, \Delta_m, v^{S,m}) \begin{pmatrix} A_{S,m} \\ B_{S,m} \end{pmatrix} = T_1 D_N(W_{N,l} + W_S, v^{N,r}) \begin{pmatrix} A_{N,r} \\ B_{N,r} \end{pmatrix} \\ &\Leftrightarrow \begin{pmatrix} A_{N,r} \\ B_{N,r} \end{pmatrix} = D_N(-W_{N,l} - W_S, v^{N,r}) T_1 T_2 D_S(W_{N,l} + W_S, \Delta_m, v^{S,m}) \begin{pmatrix} A_{S,m} \\ B_{S,m} \end{pmatrix}. \end{aligned} \quad (\text{A25})$$

The fourth intersection is at $y = W_{N,l} + W_{N,r} + W_S$ and is between the right normal section and the right superconducting region. Here, we require:

$$\begin{aligned} \Psi_{N,r}(W_{N,l} + W_{N,r} + W_S) &= \Psi_{S,r}(W_{N,l} + W_{N,r} + W_S) \\ &\Leftrightarrow T_1 D_N(W_{N,l} + W_{N,r} + W_S, v^{N,r}) \begin{pmatrix} A_{N,r} \\ B_{N,r} \end{pmatrix} = A_{S,r} e^{-(W_{N,l} + W_{N,r} + W_S)\Delta/|v^{S,r}|} \begin{pmatrix} i \operatorname{sgn}(v^{S,r}) e^{-i\theta} \\ 1 \end{pmatrix}. \end{aligned} \quad (\text{A26})$$

Using Eqs. (A19), (A21), (A25), and $D_N(W_1, v) D_N(W_2, v) = D_N(W_1 + W_2, v)$, $T_1 D_N(W, v) T_1 = D_N(-W, v)$, and equivalently for D_S , the left hand side of Eq. (A26) becomes:

$$D_N(-W_{N,r}, v^{N,r}) T_2 D_S(W_S, \Delta_m, v^{S,m}) T_2^{-1} D_N(-W_{N,l}, v^{N,l}) \begin{pmatrix} -i \operatorname{sgn}(v^{S,l}) e^{i\theta} \\ 1 \end{pmatrix}. \quad (\text{A27})$$

Now, we require that the ratio between the first and second element of the vector defined in Eq. (A27) equals the ratio on the right hand side of Eq. (A26). This gives:

$$i \operatorname{sgn}(v^{S,r}) e^{-i\theta} = -ie^{-2iW_{N,r}\Delta_z/v^{N,r}} e^{-i\phi} \frac{e^{2iW_{N,l}\Delta_z/v^{N,l}} \left(-1 + e^{2W_S\Delta_m/v^{S,m}} \right) + e^{i\theta} e^{i\phi} \operatorname{sgn}(v^{S,l}) \left(1 + e^{2W_S\Delta_m/v^{S,m}} \right)}{e^{2iW_{N,l}\Delta_z/v^{N,l}} \left(1 + e^{2W_S\Delta_m/v^{S,m}} \right) + e^{i\theta} e^{i\phi} \operatorname{sgn}(v^{S,l}) \left(-1 + e^{2W_S\Delta_m/v^{S,m}} \right)}. \quad (\text{A28})$$

After some simplification, and using $\text{sgn}(v^{N,l}) = \text{sgn}(v^{N,r}) = \text{sgn}(v^{S,l}) = \text{sgn}(v^{S,m}) = \text{sgn}(v^{S,r})$, we obtain:

$$\cos\left(\theta - \Delta_Z \left[\frac{W_{N,l}}{v^{N,l}} + \frac{W_{N,r}}{v^{N,r}}\right]\right) + \tanh\left(\frac{W_S \Delta_m}{|v^{S,m}|}\right) \cos\left(\phi - \Delta_Z \left[\frac{W_{N,l}}{v^{N,l}} - \frac{W_{N,r}}{v^{N,r}}\right]\right) = 0. \quad (\text{A29})$$

For simplicity, we assume $\Delta_l = \Delta_m = \Delta_r = \Delta_0$ in all numerical calculations. We assume $v^{N,l} = v^{N,r}$ and $v^{S,l} = v^{S,r}$. Then, to get the equation for the first branch, set $v^{N,l} = v^{N,r} \equiv v_1^N$ and $v^{S,m} = v_1^{S,m}$ [see Eq. (A6)]. For the equation of the second branch, set $v^{N,l} = v^{N,r} = -v_2^N$ and $v^{S,m} = -v_2^{S,m}$ [see Eq. (A6)]. This leads us to Eq. (7). To conclude, Eq. (A29) gives two distinct phase transition curves. This is to be expected from the Hamiltonian defined in Eq. (A6), as it has four blocks, but the first and second, as well as the third and fourth block, are particle-hole partners. Therefore, two independent solutions remain. We emphasize again that the topological phase is the area between the two phase transition curves, thus it is crucial that the two solutions have different Fermi velocities, i.e., $v_1 \neq v_2$.

1. Area of topological phase with Zeeman field

The area A of the topological phase is given by:

$$A = \int_0^{2\pi} d\phi |\theta_1(\phi) - \theta_2(\phi)|, \quad (\text{A30})$$

with $\theta_{1,2}(\phi)$ defined by Eq. (7) (assuming $W_{N,l} = W_{N,r} \equiv W_N$). To get an analytical estimate of the area, assume $\tanh(W_S \Delta_m / v_j^{S,m}) \ll 1$, such that the arccos-function can be expanded:

$$\theta_j(\phi) \approx \frac{\pi}{2} + \cos \phi \tanh\left(\frac{W_S \Delta_m}{v_j^{S,m}}\right) - \frac{2(-1)^j W_N \Delta_Z}{v_j^N}. \quad (\text{A31})$$

Therefore, the integral in Eq. (A30) is of the form

$$\begin{aligned} A &= |b_1| \int_0^{2\pi} d\phi |\cos \phi + b_2| \\ &= |b_1| \left[4\sqrt{1-b_2^2} + 2b_2\pi - 4b_2 \arccos(b_2) \right] \text{ if } |b_1| < 1, \end{aligned} \quad (\text{A32})$$

with

$$b_1 = \tanh\left(\frac{W_S \Delta_m}{v_1^{S,m}}\right) - \tanh\left(\frac{W_S \Delta_m}{v_2^{S,m}}\right), \quad (\text{A33})$$

$$b_2 = -\frac{2W_N \Delta_Z \left(\frac{1}{v_1^N} + \frac{1}{v_2^N}\right)}{b_1}. \quad (\text{A34})$$

Assuming that $W_N \Delta_Z / v_j^N \ll 1$, Eq. (A32) can be expanded in powers of Δ_Z , giving

$$\begin{aligned} A &\approx 4 \left| \tanh\left(\frac{W_S \Delta_m}{v_1^{S,m}}\right) - \tanh\left(\frac{W_S \Delta_m}{v_2^{S,m}}\right) \right| \\ &\quad + \frac{8 \left(\frac{1}{v_1^N} + \frac{1}{v_2^N}\right)^2 W_N^2}{\left| \tanh\left(\frac{W_S \Delta_m}{v_1^{S,m}}\right) - \tanh\left(\frac{W_S \Delta_m}{v_2^{S,m}}\right) \right|} \Delta_Z^2, \end{aligned} \quad (\text{A35})$$

which means that the area increases quadratically with Δ_Z . However, it was assumed that the induced superconducting gaps were independent of Δ_Z . Realistically, the induced gap decreases when a magnetic field is applied. Depending on the system parameters, this decrease of the superconducting gap can lead to an overall decrease of the area of the topological phase. However, since we consider only small magnetic fields (compared to the critical field of the superconductor), we assume that the decrease of the superconducting gap is negligible.

Appendix B: Discretized Hamiltonian

1. Finite geometry

The Hamiltonians given in the main text are discretized on a square lattice with a lattice spacing a . The Nambu basis in the finite geometry is given by

$$c_{n,m} = \left(c_{\uparrow,n,m} \quad c_{\downarrow,n,m} \quad c_{\uparrow,n,m}^\dagger \quad c_{\downarrow,n,m}^\dagger \right)^T, \quad (\text{B1})$$

where $n, m \in \mathbb{Z}$ and $c_{s,n,m}^\dagger$ creates a particle with spin s at position $(x, y) = (na, ma)$. The full Hamiltonian in the finite geometry is [106]:

$$\bar{H} = \frac{1}{2} (\bar{H}_{\text{eff}} + \bar{H}_b + \bar{H}_4 + \bar{H}_{\text{SC}} + \bar{H}_Z) \quad (\text{B2})$$

$$\begin{aligned}
& \bar{H}_{\text{eff}} + \bar{H}_b + \bar{H}_4 \\
&= \sum_{n=0}^{N_x-1} \sum_{m=0}^{N_y-1} c_{n,m}^\dagger \left(\frac{2t}{a^2} - \frac{\mu}{2} + \frac{\mu_{b,m}}{2} + \frac{10\beta}{a^4} \right) \tau_z c_{n,m} \\
&+ \sum_{n=1}^{N_x-1} \sum_{m=0}^{N_y-1} c_{n,m}^\dagger \left[-\frac{t}{a^2} - \frac{4i(\alpha + \alpha_a)}{a^3} \sigma_y - \frac{8\beta}{a^4} \right] \tau_z c_{n-1,m} \\
&+ \sum_{n=0}^{N_x-1} \sum_{m=1}^{N_y-1} c_{n,m}^\dagger \left[-\frac{t}{a^2} \tau_z - \frac{4i(\alpha + \alpha_a)}{a^3} \sigma_x - \frac{8\beta}{a^4} \tau_z \right] c_{n,m-1} \\
&+ \sum_{n=2}^{N_x-1} \sum_{m=0}^{N_y-1} c_{n,m}^\dagger \left[\frac{i(-\alpha + \alpha_a)}{a^3} \sigma_y + \frac{\beta}{a^4} \right] \tau_z c_{n-2,m} \\
&+ \sum_{n=0}^{N_x-1} \sum_{m=2}^{N_y-1} c_{n,m}^\dagger \left[\frac{i(-\alpha + \alpha_a)}{a^3} \sigma_x + \frac{\beta}{a^4} \tau_z \right] c_{n,m-2} \\
&+ \sum_{n=1}^{N_x-1} \sum_{m=1}^{N_y-1} c_{n,m}^\dagger \left[\frac{i(3\alpha + \alpha_a)}{a^3} (\sigma_x + \sigma_y \tau_z) + \frac{2\beta}{a^4} \tau_z \right] c_{n-1,m-1} \\
&+ \sum_{n=0}^{N_x-2} \sum_{m=1}^{N_y-1} c_{n,m}^\dagger \left[\frac{i(3\alpha + \alpha_a)}{a^3} (\sigma_x - \sigma_y \tau_z) + \frac{2\beta}{a^4} \tau_z \right] c_{n+1,m-1} \\
&+ \text{H.c.}, \tag{B3}
\end{aligned}$$

with N_x and N_y the number of lattice points in x and y direction respectively, $t = \hbar^2/2m^*$, and

$$\mu_{b,m} = \begin{cases} \mu_b & \text{if } m_b - \frac{N_b}{2} \leq m < m_b + \frac{N_b}{2}, \\ 0 & \text{otherwise,} \end{cases} \tag{B4}$$

where $m_b \in \{N_{S,1}, N_{S,1} + N_{N,1}, N_{S,1} + N_{S,m} + N_{N,1}, N_y - N_{S,r}\}$, $N_{S,1}$ ($N_{S,r}$) is the number of lattice points in y direction in the left (right) superconductor, $N_{S,m}$ is the number of lattice points in y direction in the middle superconductor, $N_{N,1}$ ($N_{N,r}$) is the number of lattice points in y direction in the left (right) normal conducting regions, $N_y = N_{S,1} + N_{S,m} + N_{S,r} + N_{N,1} + N_{N,r}$, and N_b is the number of lattice points in y direction in the barrier. Throughout we set $N_b = 2$. We relate the widths to the number of lattice points as follows:

$$L_x = (N_x - 1) a, \tag{B5}$$

$$L_y = (N_y - 1) a, \tag{B6}$$

$$W_{N,1} = (N_{N,1} - 1) a, \tag{B7}$$

$$W_{N,r} = (N_{N,r} - 1) a, \tag{B8}$$

$$W_S = (N_{S,m} - 1) a. \tag{B9}$$

Furthermore, the term describing the induced pairing potential due to the superconductor is

$$\bar{H}_{\text{SC}} = \sum_{n=0}^{N_x-1} \sum_{m=0}^{N_y-1} c_{n,m}^\dagger \frac{i\sigma_y}{2} (\Delta_m^* \tau_+ - \Delta_m \tau_-) c_{n,m}, \tag{B10}$$

$$\Delta_m = \begin{cases} \Delta_l e^{-i\theta} & \text{if } 0 \leq m < N_{S,1}, \\ \Delta_m e^{i\phi} & \text{if } N_{S,1} + N_{N,1} \leq m < N_{S,1} + N_{S,m} + N_{N,1}, \\ \Delta_r e^{i\theta} & \text{if } N_y - N_{S,r} \leq m < N_y, \\ 0 & \text{otherwise.} \end{cases} \tag{B11}$$

The Zeeman term is given by

$$\bar{H}_Z = \sum_{n=0}^{N_x-1} \sum_{m=0}^{N_y-1} c_{n,m}^\dagger \Delta_{Z,m} \sigma_x \tau_z c_{n,m}, \tag{B12}$$

$$\Delta_{Z,m} = \begin{cases} \Delta_Z & \text{if } N_{S,1} \leq m < N_{S,1} + N_{N,1}, \\ & \text{or } N_y - N_{S,r} - N_{N,r} \leq m < N_y - N_{S,r}, \\ 0 & \text{otherwise.} \end{cases} \tag{B13}$$

We note that the finite geometry is only used for Figs. 2(d) and 9. All other calculations are done in the semi-infinite geometry.

2. Semi-infinite geometry

For the semi-infinite geometry, we assume that the junction has an infinite extent in x direction (with periodic boundary conditions). Therefore, the momentum k_x along the x axis is a good quantum number. The corresponding Nambu basis is:

$$c_{k_x, m} = \left(c_{\uparrow, k_x, m} \quad c_{\downarrow, k_x, m} \quad c_{\uparrow, -k_x, m}^\dagger \quad c_{\downarrow, -k_x, m}^\dagger \right)^T, \tag{B14}$$

where $c_{s, k_x, m}^\dagger$ creates a particle at position $y = ma$ with spin s and momentum k_x in the x direction. The Hamiltonian in the semi-infinite geometry is [106]:

$$\tilde{H} = \frac{1}{2} \int_{-\infty}^{\infty} dk_x \left[\tilde{H}_{\text{eff}}(k_x) + \tilde{H}_b(k_x) + \tilde{H}_4(k_x) + \tilde{H}_{SC}(k_x) + \tilde{H}_Z(k_x) \right], \quad (\text{B15})$$

$$\begin{aligned} \tilde{H}_{\text{eff}}(k_x) + \tilde{H}_b(k_x) + \tilde{H}_4(k_x) &= \sum_{m=0}^{N_y-1} c_{k_x,m}^\dagger \left\{ \frac{t[2 - \cos(k_x a)]}{a^2} - \frac{\mu}{2} + \frac{\mu_{b,m}}{2} + \frac{\beta}{a^4} [10 - 8 \cos(k_x a) + \cos(2k_x a)] \right. \\ &\quad \left. - \frac{4(\alpha + \alpha_a)}{a^3} \sin(k_x a) \sigma_y + \frac{-\alpha + \alpha_a}{a^3} \sin(2k_x a) \sigma_y \right\} \tau_z c_{k_x,m} \\ &\quad + \sum_{m=1}^{N_y-1} c_{k_x,m}^\dagger \left\{ -\frac{t}{a^2} \tau_z + \frac{4\beta}{a^4} [-2 + \cos(k_x a)] \tau_z + \frac{2(3\alpha + \alpha_a)}{a^3} \sin(k_x a) \sigma_y \tau_z \right. \\ &\quad \left. + \frac{2i}{a^3} [(3\alpha + \alpha_a) \cos(k_x a) - 2(\alpha + \alpha_a)] \sigma_x \right\} c_{k_x,m-1} \\ &\quad + \sum_{m=2}^{N_y-1} c_{k_x,m}^\dagger \left(\frac{i(-\alpha + \alpha_a)}{a^3} \sigma_x + \frac{\beta}{a^4} \tau_z \right) c_{k_x,m-2} + \text{H.c.} \end{aligned} \quad (\text{B16})$$

The induced superconducting pairing potential is described by

$$\tilde{H}_{SC}(k_x) = \sum_{m=0}^{N_y-1} c_{k_x,m}^\dagger \frac{i\sigma_y}{2} (\Delta_m \tau_+ - \Delta_m^* \tau_-) c_{k_x,m}, \quad (\text{B17})$$

where Δ_m is defined in Eq. (B11). The Zeeman term is:

$$\tilde{H}_Z(k_x) = \sum_{m=0}^{N_y-1} \Delta_{Z,m} c_{k_x,m}^\dagger \sigma_x \tau_z c_{k_x,m}, \quad (\text{B18})$$

where $\Delta_{Z,m}$ is defined in Eq. (B13).

3. Parameters

In this subsection, we give the numerical values for all parameters used to generate Figs. 2 and 3. For Fig. 2, all parameters are given in units of $t = \hbar^2/2m^*$ and the lattice spacing a . The parameters are $a = 4$ nm, $\alpha = 0.68ta$, $\beta = 0.49ta^2$, $\mu = 0.065ta^{-2}$. In Fig. 2(a)-2(c) $\Delta_0 = 0.007ta^{-2}$, $N_{N,1} = N_{N,r} = 8$, and $N_S = 33$. In Fig. 2(d) $\Delta_0 = 0.022ta^{-2}$, $N_{N,1} = N_{N,r} = 6$, and $N_S = 18$. In Fig. 2(a), the outer superconductors are assumed to be infinitely wide (in y direction), while in Figs. 2(b) and 2(c), their widths are finite, given by $N_{S,1} = N_{S,r} = 300$. In Fig. 2(d) the widths of the outer superconductors are $N_{S,1} = N_{S,r} = 100$ and the system has a finite extent in x direction of $N_x = 500$. The potential barriers in Fig. 2(b) are $\mu_b = 0.035ta^{-2}$ and $\mu_b = 0.165ta^{-2}$. The potential barrier in Fig. 2(c) is $\mu_b = 0.055ta^{-2}$ and in Fig. 2(d) $\mu_b = 0$. The superconducting coherence lengths $\xi_j = v_j/\Delta_0$ in Figs. 2(a)-2(c) are $\xi_1 = 50a$ and $\xi_2 = 41a$. In 2(d) $\xi_1 = 30a$ and $\xi_2 = 13a$. For Figs. 2(a)-2(d), the Fermi wavelengths $\lambda_j = 2\pi/k_j$ are $\lambda_1 = 28a$ and $\lambda_2 = 19a$.

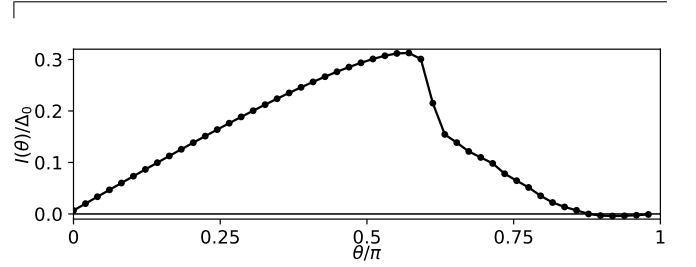


FIG. 5. Current-phase relation of an SNSNS junction, where the superconducting phase differences are $-\theta/2$, $\phi = 0$, $\theta/2$ for the left, middle, and right superconductors respectively. This current-phase relation is more complicated than the simple form for an SNS junction defined in Eq. (C2).

For Fig. 3 the parameters are instead given in units of the lattice spacing a and the energy scale $E_0 = 37$ meV, which is an energy scale discussed in Ref. [106]. In these units, the parameters are $a = 1.85$ nm, $t = \hbar^2/2m^* = 4.9E_0a^2$, $\alpha = 0.81E_0a^3$, $\alpha_a = 0.1E_0a^3$, $\beta = 0.17E_0a^4$, $\mu = 0.2E_0$, $\Delta_0 = 0.013E_0$, $\mu_b = 0.33E_0$, $N_{N,1} = N_{N,r} = 40$, $N_S = 95$, and $N_{S,1} = N_{S,r} = 500$. The superconducting coherence lengths are $\xi_1 = 161a$ and $\lambda_2 = 143a$ and the Fermi wavelengths are $\lambda_1 = 32a$ and $\lambda_2 = 30a$.

Appendix C: Transparency calculation

In this Appendix, we show how the transparency of the junction is calculated. We estimate the transparency using the current-phase relation $I(\rho)$, which is proportional to [129]:

$$I(\rho) \propto \frac{\partial}{\partial \rho} \int_{E < 0} dk_x E(k_x, \rho), \quad (\text{C1})$$

where ρ is the superconducting phase difference and $E(k_x, \rho)$ is the energy spectrum calculated in the semi-infinite geometry. The current-phase relation of an

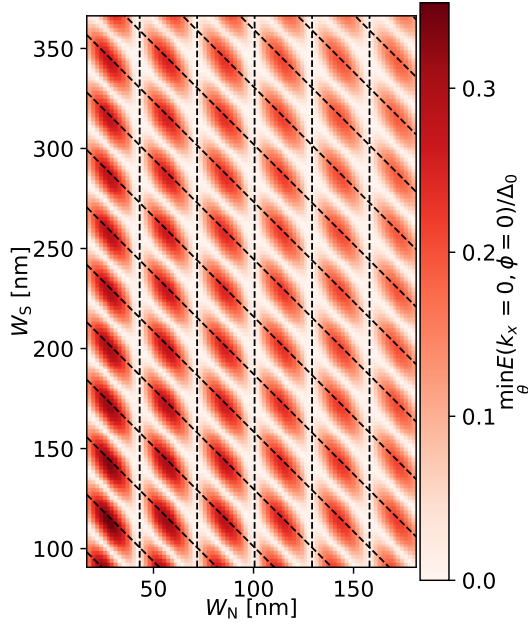


FIG. 6. Minimum energy varying θ in the semi-infinite geometry at $k_x = 0$ and $\phi = 0$. This is the same plot as Fig. 2(c), however here using realistic parameters for Ge. The parameters are as in Fig. 3 and the tunneling barrier is fixed to 5.18 meV.

SNSNS junction is not uniquely defined because there are two independent superconducting phase differences. For simplicity, we set $\phi = 0$. This, however, results in a rather complicated current-phase relation for an SNSNS junction; see Fig. 5. It is not clear how this current-phase relation depends on the transparency. In contrast, for an SNS junction, the transparency is well approximated by [129]:

$$I(\rho) = I_0 \frac{\sin(\rho)}{\sqrt{1 - \tau \sin^2(\rho/2)}}, \quad (\text{C2})$$

where I_0 is a real parameter. Therefore, we estimate the transparency of the system using the current-phase relation of an SNS junction with normal conducting section width $W_N \equiv W_{N,l} = W_{N,r}$. The transparency τ is then obtained by comparing the ratio of the first and second harmonics of Eqs. (C1) and (C2).

Appendix D: Ideal junction geometry

The analytic calculation of the phase diagram (see Ref. [124] and Appendix A) assumes perfect transparency, which is apparent from the Hamiltonian in Eq. (A6), as it does not couple left and right movers. Phenomenologically, such a coupling can be introduced by adapting the linearized Hamiltonian of Appendix A

as follows:

$$H' = H + c^\dagger(k_y) \begin{pmatrix} 0 & 0 & 0 & H_T \\ 0 & 0 & H_T & 0 \\ 0 & H_T & 0 & 0 \\ H_T & 0 & 0 & 0 \end{pmatrix} c(k_y), \quad (\text{D1})$$

where the Hamiltonian H is defined in Eq. (A6) and

$$H_T = \begin{pmatrix} \delta & 0 \\ 0 & \delta \end{pmatrix}, \quad (\text{D2})$$

where δ labels the overlap between the left- and right-movers. In this ansatz, we assume that spin is conserved. Perturbatively, the overlap δ can be estimated as the overlap between the left- and right-moving wave functions calculated for the uncoupled system in Appendix A. For the following derivation, we focus on the spin + branch, noting that the derivation for the spin - branch is equivalent. By defining the wave functions

$$\Psi_R = (R_+(k_y) \ L_-^\dagger(-k_y))^T, \quad (\text{D3})$$

$$\Psi_L = (L_+(k_y) \ R_-^\dagger(-k_y))^T, \quad (\text{D4})$$

we want a condition for which parameters the scattering has a negligible impact. This is the case if there is no overlap between left- and right-movers:

$$0 = \langle \Psi_R | V | \Psi_L \rangle, \quad (\text{D5})$$

where V is the potential that couples the left- and right-movers, i.e., the potential barrier at the SN interface. For simplicity, we assume a Dirac δ potential at each intersection:

$$V(y) = V_0 [\delta(y) + \delta(y - W_N) + \delta(y - W_N - W_S) + \delta(y - 2W_N - W_S)], \quad (\text{D6})$$

where V_0 is real, $W_N = W_{N,l} = W_{N,r}$ is the width of each normal conducting section, and W_S is the width of the middle superconducting section. Since the largest extent of the topological phase is at $\phi = 0$ (or $\phi = \pi$), we set $\phi = 0$. Furthermore, we set $\Delta_Z = 0$ and assume that the Fermi velocities and Fermi momenta are equal in all sectors, i.e., $v_j^{S,l} = v_j^{S,m} = v_j^{S,r} = v_j^{N,l} = v_j^{N,r} \equiv v_j$ and $k_j^{S,l} = k_j^{S,m} = k_j^{S,r} = k_j^{N,l} = k_j^{N,r} \equiv k_j$ for $j = 1, 2$. We note that in this step, the oscillating prefactors $e^{\pm ik_{1,2}y}$ in Eq. (A2) must be taken into account explicitly. At the first interface, which is at $y = 0$, the wave functions are [see Eq. (A19)]:

$$\Psi_L(0) = \begin{pmatrix} ie^{i\theta_L} \\ 1 \end{pmatrix}, \quad \Psi_R(0) = \begin{pmatrix} -ie^{i\theta_R} \\ 1 \end{pmatrix}, \quad (\text{D7})$$

where θ_L and θ_R can be expressed using Eq. (7):

$$e^{i\theta_L} = -\tanh\left(\frac{W_S\Delta_m}{v_2}\right) + i\sqrt{1 - \tanh^2\left(\frac{W_S\Delta_m}{v_2}\right)}, \quad (\text{D8})$$

$$e^{-i\theta_R} = -\tanh\left(\frac{W_S\Delta_m}{v_1}\right) - i\sqrt{1 - \tanh^2\left(\frac{W_S\Delta_m}{v_1}\right)}. \quad (\text{D9})$$

At the second interface at $y = W_N$, one gets:

$$\Psi_L(W_N) = e^{-ik_2W_N}\Psi_L(0), \quad (\text{D10})$$

$$\Psi_R(W_N) = e^{ik_1W_N}\Psi_R(0). \quad (\text{D11})$$

At the third interface at $y = W_N + W_S$ the wave functions are [see Eq. (A25)]:

$$\Psi_L(W_N + W_S) = e^{-ik_2(W_N + W_S)}M(-v_2)\Psi_L(0), \quad (\text{D12})$$

$$\Psi_R(W_N + W_S) = e^{ik_1(W_N + W_S)}M(v_1)\psi_R(0), \quad (\text{D13})$$

with

$$M(v) = \begin{pmatrix} \cosh\left(\frac{W_S\Delta_m}{v}\right) & -i\sinh\left(\frac{W_S\Delta_m}{v}\right) \\ i\sinh\left(\frac{W_S\Delta_m}{v}\right) & \cosh\left(\frac{W_S\Delta_m}{v}\right) \end{pmatrix}. \quad (\text{D14})$$

Finally, at the fourth interface at $y = 2W_N + W_S$, one obtains

$$\Psi_L(2W_N + W_S) = e^{-ik_2W_N}\Psi_L(W_N + W_S), \quad (\text{D15})$$

$$\Psi_R(2W_N + W_S) = e^{ik_1W_N}\Psi_R(W_N + W_S). \quad (\text{D16})$$

Therefore, Eq. (D5) becomes:

$$0 = \left(1 + e^{-i(k_1+k_2)W_N}\right) \left(i e^{-i\theta_R} - 1\right) \\ \times \left(1 + e^{-i(k_1+k_2)(W_N+W_S)} [M(v_1)]^\dagger M(-v_2)\right) \begin{pmatrix} i e^{i\theta_L} \\ 1 \end{pmatrix}. \quad (\text{D17})$$

Finally, this gives the condition that the overlap of left- and right-movers is minimized when

$$0 = 2i e^{-i(k_1+k_2)(W_N+W_S)} \frac{e^{W_S\Delta_m/v_1} - e^{W_S\Delta_m/v_2}}{(1 + i e^{W_S\Delta_m/v_1})(1 - i e^{W_S\Delta_m/v_2})} \\ \times \left(1 + e^{-i(k_1+k_2)W_N}\right) \left(-1 + e^{i(k_1+k_2)(W_N+W_S)}\right). \quad (\text{D18})$$

Thus, either one of the following conditions must be fulfilled:

$$0 = 1 + e^{-i(k_1+k_2)W_N} \quad \text{or} \quad 0 = -1 + e^{i(k_1+k_2)(W_N+W_S)}, \quad (\text{D19})$$

which are the conditions in Eq. (8). We show the existence of an ideal junction geometry for the toy-model parameters in Fig. 2(c) and for realistic Ge parameters in Fig. 6. In both cases, the analytically calculated lines [see Eq. (8)] deviate systematically from the numerically

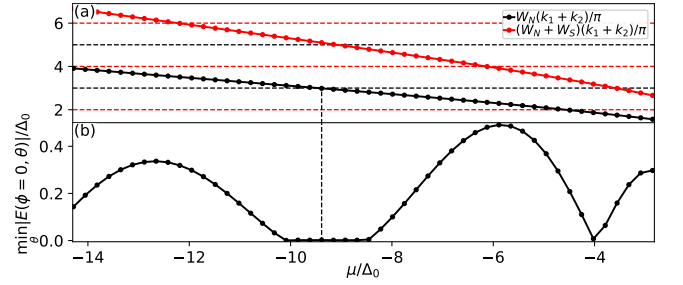


FIG. 7. For fixed widths W_N and W_S , the chemical potential μ is varied to tune the system such that one of the conditions of Eq. (8) is fulfilled. (a) The black dots indicate $\frac{W_N(k_1+k_2)}{\pi}$, which has to be an odd integer (indicated by the horizontal black dashed lines) to satisfy one of the ideal junction conditions in Eq. (8). The red dots indicate $\frac{(W_N+W_S)(k_1+k_2)}{\pi}$, which has to be an even integer (indicated by the horizontal red dashed lines) to satisfy Eq. (8). By varying the chemical potential μ , the Fermi momenta k_1 and k_2 are varied, while W_N and W_S are kept constant. (b) Minimum energy $\min_\theta |E(\phi=0, \theta)|$ in the semi-infinite geometry at $k_x = 0$ and $\phi = 0$. A topological phase only exists if this minimum energy is zero. The vertical dashed line indicates where one of the conditions of Eq. (8) is satisfied. The parameters are as in Fig. 2(c). The width of the normal section is $W_N = 68$ nm (i.e., $N_N = 13$) and $W_S = 48$ nm (i.e., $N_S = 18$).

calculated values. There are several reasons why the numerically observed ideal junction geometry is slightly different compared to the analytically expected conditions. For instance, although we define a relation between N_S and W_S (and between N_N and W_N) in Eqs. (B7)-(B9), it is only a convention and not uniquely defined. A further complication comes from the potential barrier, which is not a Dirac delta potential, but has a finite extent in the numerical calculation.

Although no longer giving simple analytical conditions, we have checked numerically that qualitatively, the same conditions on the ideal junction geometry still apply even for the case when $W_{N,l} \neq W_{N,r}$, or having different tunneling barrier heights at each intersection, or when there are different Fermi velocities and wave vectors in each section.

We mention in the main text that in an experiment, W_N and W_S are fixed after fabrication. However, by gating the sample, the chemical potential μ is changed, which affects the Fermi momenta k_1 and k_2 . This changes the conditions on the ideal junction geometry, see Eq. (8). While it is not always reasonable to change the chemical potential such that both conditions in Eq. (8) are fulfilled, it is possible to change the chemical potential such that at least one of the conditions in Eq. (8) is satisfied, see Fig. 7.

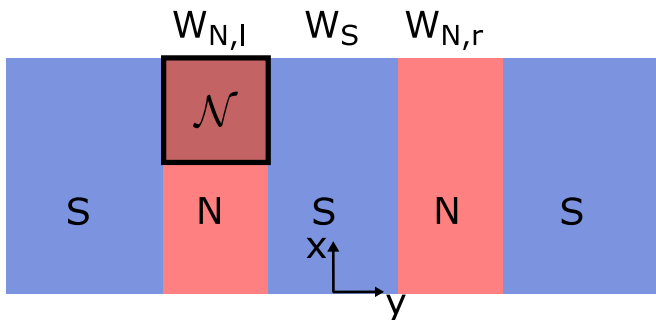


FIG. 8. Definition of the area \mathcal{N} in Eq. (E1). It is a square of side length $W_{N,l}$.

Appendix E: Local density of states

The integrated local density of states LDOS for Fig. 2(d) is defined as follows:

$$\text{LDOS} = \sum_n \iint_{\mathcal{N}} dx dy \int_{-\mathcal{E}}^{\mathcal{E}} dE f(E - E_n) |\Psi_n(x, y)|^2, \quad (\text{E1})$$

where n labels all eigenstates of the system, their energy being E_n and their wave function Ψ_n , \mathcal{N} is the area over which to integrate, \mathcal{E} is a parameter that defines the boundary of the energy integral [we use $\mathcal{E}/\Delta_0 = 0.47$ for Fig. 2(d)], and $f(E - E_n)$ is a broadening function. Using the same coordinate system as in the main text, we define $\mathcal{N} = \{(x, y) | 0 \leq x < W_{N,l} \text{ and } -W_{N,l} - W_S/2 \leq y < -W_S/2\}$, see Fig. 8. The broadening function is defined as a Cauchy distribution:

$$f(E) = \frac{1}{\pi} \frac{\nu}{E^2 + \nu^2}, \quad (\text{E2})$$

where ν is the broadening coefficient. In the inset of Fig. 2(d), the broadening coefficient of the green curve is $\overline{\Delta E}$, $2\overline{\Delta E}$ for the blue curve, and $4\overline{\Delta E}$ for the orange curve. Here, $\overline{\Delta E}$ is the numerically determined average level spacing, which is $1.9 \mu\text{eV}$.

Appendix F: Wave function of Majorana bound states

In Fig. 2(d), we show a profile cut through an MBS probability density. We show the full two-dimensional MBS probability density in Fig. 9. The MBSs are localized at opposite ends and, depending on the superconducting phase, values are more localized in one or the other junction. We note that the large portion of the MBS wave function is located under the bulk superconductor, which allows one to minimize the overlap between two MBSs. These MBSs are well localized and hardly overlap in spite of a relatively small topological gap.

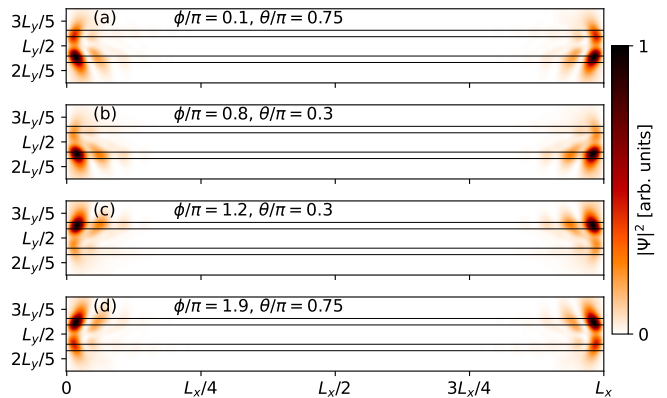


FIG. 9. The probability density of MBSs for different points in the phase diagram. All parameters are as in Fig. 2(d), except the superconducting phase differences ϕ and θ , which are indicated in the corresponding panel. We note that, depending on these phases, the MBSs have larger support in one or the other junction, breaking the symmetry between them.

Appendix G: Energy spectrum for germanium

In this Appendix we show the energy spectrum $E(k_x)$ in the semi-infinite geometry for realistic Ge parameters in both the trivial and topological phase, as well as at the topological phase transition; see Fig. 10. The energy spectrum shows that in the topological phase there are many in-gap states, however, as discussed in the main text, in finite length systems the trivial states are de-

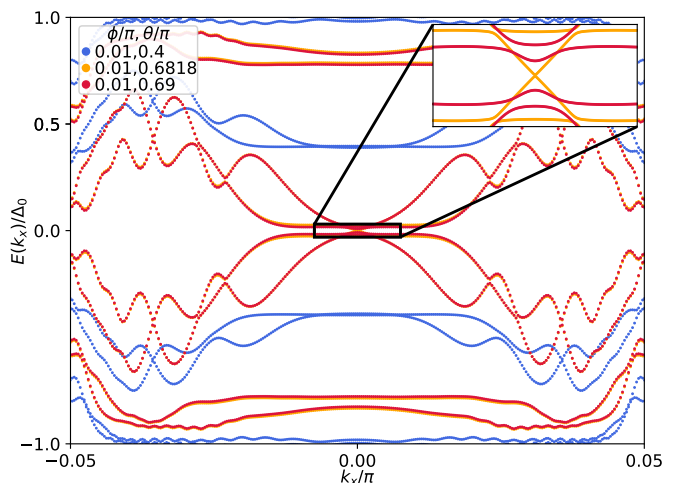


FIG. 10. Energy spectrum $E(k_x)$ in the semi-infinite geometry. The parameters are for a realistic Ge system and are the same as for Fig. 3. The data represented by the blue dots is for superconducting phase differences ϕ and θ deep in the trivial phase, the yellow dots are at the phase transition, and the red dots are in the topological phase.

localized over the full length of the junction, whereas

MBSs are localized at the junction ends and therefore more prominent in the LDOS.

-
- [1] A. Y. Kitaev, Unpaired Majorana fermions in quantum wires, *Physics-Uspekhi* **44**, 131 (2001).
- [2] M. Leijnse and K. Flensberg, Introduction to topological superconductivity and Majorana fermions, *Semiconductor Science and Technology* **27**, 124003 (2012).
- [3] X.-L. Qi and S.-C. Zhang, Topological insulators and superconductors, *Rev. Mod. Phys.* **83**, 1057 (2011).
- [4] C. Beenakker, Search for Majorana Fermions in Superconductors, *Annual Review of Condensed Matter Physics* **4**, 113 (2013).
- [5] M. Sato and S. Fujimoto, Majorana fermions and topology in superconductors, *Journal of the Physical Society of Japan* **85**, 072001 (2016).
- [6] R. Pawlak, S. Hoffman, J. Klinovaja, D. Loss, and E. Meyer, Majorana fermions in magnetic chains, *Progress in Particle and Nuclear Physics* **107**, 1 (2019).
- [7] K. Laubscher and J. Klinovaja, Majorana bound states in semiconducting nanostructures, *Journal of Applied Physics* **130**, 081101 (2021).
- [8] A. Kitaev, Fault-tolerant quantum computation by anyons, *Annals of Physics* **303**, 2 (2003).
- [9] C. Nayak, S. H. Simon, A. Stern, M. Freedman, and S. Das Sarma, Non-Abelian anyons and topological quantum computation, *Rev. Mod. Phys.* **80**, 1083 (2008).
- [10] S. R. Elliott and M. Franz, Colloquium: Majorana fermions in nuclear, particle, and solid-state physics, *Rev. Mod. Phys.* **87**, 137 (2015).
- [11] G. Kells, D. Meidan, and P. W. Brouwer, Near-zero-energy end states in topologically trivial spin-orbit coupled superconducting nanowires with a smooth confinement, *Phys. Rev. B* **86**, 100503 (2012).
- [12] E. J. H. Lee, X. Jiang, R. Aguado, G. Katsaros, C. M. Lieber, and S. De Franceschi, Zero-Bias Anomaly in a Nanowire Quantum Dot Coupled to Superconductors, *Phys. Rev. Lett.* **109**, 186802 (2012).
- [13] D. Rainis, L. Trifunovic, J. Klinovaja, and D. Loss, Towards a realistic transport modeling in a superconducting nanowire with Majorana fermions, *Phys. Rev. B* **87**, 024515 (2013).
- [14] D. Roy, N. Bondyopadhyaya, and S. Tewari, Topologically trivial zero-bias conductance peak in semiconductor majorana wires from boundary effects, *Phys. Rev. B* **88**, 020502 (2013).
- [15] A. Ptok, A. Kobińska, and T. Domański, Controlling the bound states in a quantum-dot hybrid nanowire, *Phys. Rev. B* **96**, 195430 (2017).
- [16] C.-X. Liu, J. D. Sau, T. D. Stanescu, and S. Das Sarma, Andreev bound states versus Majorana bound states in quantum dot-nanowire-superconductor hybrid structures: Trivial versus topological zero-bias conductance peaks, *Phys. Rev. B* **96**, 075161 (2017).
- [17] C. Moore, T. D. Stanescu, and S. Tewari, Two-terminal charge tunneling: Disentangling Majorana zero modes from partially separated Andreev bound states in semiconductor-superconductor heterostructures, *Phys. Rev. B* **97**, 165302 (2018).
- [18] C. Moore, C. Zeng, T. D. Stanescu, and S. Tewari, Quantized zero-bias conductance plateau in semiconductor-superconductor heterostructures without topological Majorana zero modes, *Phys. Rev. B* **98**, 155314 (2018).
- [19] C. Reeg, O. Dmytruk, D. Chevallier, D. Loss, and J. Klinovaja, Zero-energy Andreev bound states from quantum dots in proximitized Rashba nanowires, *Phys. Rev. B* **98**, 245407 (2018).
- [20] A. Vuik, B. Nijholt, A. R. Akhmerov, and M. Wimmer, Reproducing topological properties with quasi-Majorana states, *SciPost Phys.* **7**, 061 (2019).
- [21] T. D. Stanescu and S. Tewari, Robust low-energy Andreev bound states in semiconductor-superconductor structures: Importance of partial separation of component Majorana bound states, *Phys. Rev. B* **100**, 155429 (2019).
- [22] B. D. Woods, J. Chen, S. M. Frolov, and T. D. Stanescu, Zero-energy pinning of topologically trivial bound states in multiband semiconductor-superconductor nanowires, *Phys. Rev. B* **100**, 125407 (2019).
- [23] J. Chen, B. D. Woods, P. Yu, M. Hocevar, D. Car, S. R. Plissard, E. P. A. M. Bakkers, T. D. Stanescu, and S. M. Frolov, Ubiquitous Non-Majorana Zero-Bias Conductance Peaks in Nanowire Devices, *Phys. Rev. Lett.* **123**, 107703 (2019).
- [24] O. A. Awoga, J. Cayao, and A. M. Black-Schaffer, Supercurrent detection of topologically trivial zero-energy states in nanowire junctions, *Phys. Rev. Lett.* **123**, 117001 (2019).
- [25] E. Prada, P. San-Jose, M. W. de Moor, A. Geresdi, E. J. Lee, J. Klinovaja, D. Loss, J. Nygård, R. Aguado, and L. P. Kouwenhoven, From Andreev to Majorana bound states in hybrid superconductor-semiconductor nanowires, *Nature Reviews Physics* **2**, 575 (2020).
- [26] P. Yu, J. Chen, M. Gomanko, G. Badawy, E. Bakkers, K. Zuo, V. Mourik, and S. Frolov, Non-Majorana states yield nearly quantized conductance in proximitized nanowires, *Nature Physics* **17**, 482 (2021).
- [27] S. Das Sarma and H. Pan, Disorder-induced zero-bias peaks in Majorana nanowires, *Phys. Rev. B* **103**, 195158 (2021).
- [28] M. Valentini, F. Peñaranda, A. Hofmann, M. Brauns, R. Hauschild, P. Krogstrup, P. San-Jose, E. Prada, R. Aguado, and G. Katsaros, Nontopological zero-bias peaks in full-shell nanowires induced by flux-tunable Andreev states, *Science* **373**, 82 (2021).
- [29] R. Hess, H. F. Legg, D. Loss, and J. Klinovaja, Local and nonlocal quantum transport due to Andreev bound states in finite Rashba nanowires with superconducting and normal sections, *Phys. Rev. B* **104**, 075405 (2021).
- [30] R. Hess, H. F. Legg, D. Loss, and J. Klinovaja, Trivial Andreev Band Mimicking Topological Bulk Gap Reopening in the Nonlocal Conductance of Long Rashba Nanowires, *Phys. Rev. Lett.* **130**, 207001 (2023).
- [31] C. Reeg and D. L. Maslov, Transport signatures of topological superconductivity in a proximity-coupled

- nanowire, Phys. Rev. B **95**, 205439 (2017).
- [32] C. Reeg, D. Loss, and J. Klinovaja, Finite-size effects in a nanowire strongly coupled to a thin superconducting shell, Phys. Rev. B **96**, 125426 (2017).
- [33] C. Reeg, D. Loss, and J. Klinovaja, Metallization of a Rashba wire by a superconducting layer in the strong-proximity regime, Phys. Rev. B **97**, 165425 (2018).
- [34] C. Reeg, D. Loss, and J. Klinovaja, Proximity effect in a two-dimensional electron gas coupled to a thin superconducting layer, Beilstein Journal of Nanotechnology **9**, 1263 (2018).
- [35] A. E. Antipov, A. Bargerbos, G. W. Winkler, B. Bauer, E. Rossi, and R. M. Lutchyn, Effects of Gate-Induced Electric Fields on Semiconductor Majorana Nanowires, Phys. Rev. X **8**, 031041 (2018).
- [36] B. D. Woods, T. D. Stanescu, and S. Das Sarma, Effective theory approach to the Schrödinger-Poisson problem in semiconductor Majorana devices, Phys. Rev. B **98**, 035428 (2018).
- [37] T. Kiendl, F. von Oppen, and P. W. Brouwer, Proximity-induced gap in nanowires with a thin superconducting shell, Phys. Rev. B **100**, 035426 (2019).
- [38] G. W. Winkler, A. E. Antipov, B. van Heck, A. A. Soluyanov, L. I. Glazman, M. Wimmer, and R. M. Lutchyn, Unified numerical approach to topological semiconductor-superconductor heterostructures, Phys. Rev. B **99**, 245408 (2019).
- [39] O. A. Awoga, J. Cayao, and A. M. Black-Schaffer, Robust topological superconductivity in weakly coupled nanowire-superconductor hybrid structures, Phys. Rev. B **105**, 144509 (2022).
- [40] M. Sato, Y. Takahashi, and S. Fujimoto, Non-Abelian Topological Order in s -Wave Superfluids of Ultracold Fermionic Atoms, Phys. Rev. Lett. **103**, 020401 (2009).
- [41] J. D. Sau, R. M. Lutchyn, S. Tewari, and S. Das Sarma, Generic New Platform for Topological Quantum Computation Using Semiconductor Heterostructures, Phys. Rev. Lett. **104**, 040502 (2010).
- [42] J. Alicea, Majorana fermions in a tunable semiconductor device, Phys. Rev. B **81**, 125318 (2010).
- [43] R. M. Lutchyn, J. D. Sau, and S. Das Sarma, Majorana Fermions and a Topological Phase Transition in Semiconductor-Superconductor Heterostructures, Phys. Rev. Lett. **105**, 077001 (2010).
- [44] Y. Oreg, G. Refael, and F. von Oppen, Helical Liquids and Majorana Bound States in Quantum Wires, Phys. Rev. Lett. **105**, 177002 (2010).
- [45] J. D. Sau, S. Tewari, R. M. Lutchyn, T. D. Stanescu, and S. Das Sarma, Non-Abelian quantum order in spin-orbit-coupled semiconductors: Search for topological Majorana particles in solid-state systems, Phys. Rev. B **82**, 214509 (2010).
- [46] A. M. Black-Schaffer and J. Linder, Majorana fermions in spin-orbit-coupled ferromagnetic Josephson junctions, Phys. Rev. B **84**, 180509 (2011).
- [47] E. Prada, P. San-Jose, and R. Aguado, Transport spectroscopy of NS nanowire junctions with Majorana fermions, Phys. Rev. B **86**, 180503 (2012).
- [48] A. M. Black-Schaffer, Edge Properties and Majorana Fermions in the Proposed Chiral d -Wave Superconducting State of Doped Graphene, Phys. Rev. Lett. **109**, 197001 (2012).
- [49] J. Klinovaja, G. J. Ferreira, and D. Loss, Helical states in curved bilayer graphene, Phys. Rev. B **86**, 235416 (2012).
- [50] J. D. Sau and S. Tewari, Topological superconducting state and Majorana fermions in carbon nanotubes, Phys. Rev. B **88**, 054503 (2013).
- [51] C. Dutreix, M. Guigou, D. Chevallier, and C. Bena, Majorana fermions in honeycomb lattices, The European Physical Journal B **87**, 296 (2014).
- [52] M. Hell, M. Leijnse, and K. Flensberg, Two-Dimensional Platform for Networks of Majorana Bound States, Phys. Rev. Lett. **118**, 107701 (2017).
- [53] F. Pientka, A. Keselman, E. Berg, A. Yacoby, A. Stern, and B. I. Halperin, Topological Superconductivity in a Planar Josephson Junction, Phys. Rev. X **7**, 021032 (2017).
- [54] G. R. Wagner and M. A. Janocko, Observation of a two-dimensional hole gas in boron-doped $\text{Si}_{0.5}\text{Ge}_{0.5}/\text{Ge}$ heterostructures, Applied Physics Letters **54**, 66 (1989).
- [55] E. Murakami, K. Nakagawa, A. Nishida, and M. Miyao, Strain-controlled Si-Ge modulation-doped FET with ultrahigh hole mobility, IEEE Electron Device Letters **12**, 71 (1991).
- [56] Y. H. Xie, D. Monroe, E. A. Fitzgerald, P. J. Silverman, F. A. Thiel, and G. P. Watson, Very high mobility two-dimensional hole gas in $\text{Si}/\text{Ge}_x\text{Si}_{1-x}/\text{Ge}$ structures grown by molecular beam epitaxy, Applied Physics Letters **63**, 2263 (1993).
- [57] T. Irisawa, M. Myronov, O. A. Mironov, E. H. C. Parker, K. Nakagawa, M. Murata, S. Koh, and Y. Shiraki, Hole density dependence of effective mass, mobility and transport time in strained Ge channel modulation-doped heterostructures, Applied Physics Letters **82**, 1425 (2003).
- [58] B. Röbner, G. Isella, and H. v. Känel, Effective mass in remotely doped Ge quantum wells, Applied Physics Letters **82**, 754 (2003).
- [59] B. Röbner, D. Chrastina, G. Isella, and H. von Känel, Scattering mechanisms in high-mobility strained Ge channels, Applied Physics Letters **84**, 3058 (2004).
- [60] V. A. Shah, A. Dobbie, M. Myronov, and D. R. Leadley, Reverse graded SiGe/Ge/Si buffers for high-composition virtual substrates, Journal of Applied Physics **107**, 064304 (2010).
- [61] C. Kloeffel, M. Trif, and D. Loss, Strong spin-orbit interaction and helical hole states in Ge/Si nanowires, Phys. Rev. B **84**, 195314 (2011).
- [62] A. Dobbie, M. Myronov, R. J. H. Morris, A. H. A. Hassan, M. J. Prest, V. A. Shah, E. H. C. Parker, T. E. Whall, and D. R. Leadley, Ultra-high hole mobility exceeding one million in a strained germanium quantum well, Applied Physics Letters **101**, 172108 (2012).
- [63] J. Foronda, C. Morrison, J. E. Halpin, S. D. Rhead, and M. Myronov, Weak antilocalization of high mobility holes in a strained Germanium quantum well heterostructure, Journal of Physics: Condensed Matter **27**, 022201 (2014).
- [64] O. A. Mironov, N. d'Ambrumenil, A. Dobbie, D. R. Leadley, A. V. Suslov, and E. Green, Fractional Quantum Hall States in a Ge Quantum Well, Phys. Rev. Lett. **116**, 176802 (2016).
- [65] M. Lodari, A. Tosato, D. Sabbagh, M. A. Schubert, G. Capellini, A. Sammak, M. Veldhorst, and G. Scappucci, Light effective hole mass in undoped Ge/SiGe quantum wells, Phys. Rev. B **100**, 041304 (2019).

- [66] G. Scappucci, C. Kloeffel, F. A. Zwanenburg, D. Loss, M. Myronov, J.-J. Zhang, S. De Franceschi, G. Katsaros, and M. Veldhorst, The germanium quantum information route, *Nature Reviews Materials* **6**, 926 (2021).
- [67] M. Lodari, N. W. Hendrickx, W. I. L. Lawrie, T.-K. Hsiao, L. M. K. Vandersypen, A. Sammak, M. Veldhorst, and G. Scappucci, Low percolation density and charge noise with holes in germanium, *Materials for Quantum Technology* **1**, 011002 (2021).
- [68] R. Mizokuchi, R. Maurand, F. Vigneau, M. Myronov, and S. De Franceschi, Ballistic One-Dimensional Holes with Strong g-Factor Anisotropy in Germanium, *Nano Letters* **18**, 4861 (2018), pMID: 29995419.
- [69] M. Myronov, J. Kycia, P. Waldron, W. Jiang, P. Barrios, A. Bogan, P. Coleridge, and S. Studenikin, Holes Outperform Electrons in Group IV Semiconductor Materials, *Small Science* **3**, 2200094 (2023).
- [70] Y. Hu, H. O. Churchill, D. J. Reilly, J. Xiang, C. M. Lieber, and C. M. Marcus, A Ge/Si heterostructure nanowire-based double quantum dot with integrated charge sensor, *Nature nanotechnology* **2**, 622 (2007).
- [71] Y. Hu, F. Kuemmeth, C. M. Lieber, and C. M. Marcus, Hole spin relaxation in Ge-Si core-shell nanowire qubits, *Nature nanotechnology* **7**, 47 (2012).
- [72] N. Ares, G. Katsaros, V. N. Golovach, J. Zhang, A. Prager, L. I. Glazman, O. G. Schmidt, and S. De Franceschi, SiGe quantum dots for fast hole spin Rabi oscillations, *Applied Physics Letters* **103**, 263113 (2013).
- [73] H. Watzinger, J. Kukučka, L. Vukušić, F. Gao, T. Wang, F. Schäffler, J.-J. Zhang, and G. Katsaros, A germanium hole spin qubit, *Nature communications* **9**, 3902 (2018).
- [74] Y. Li, S.-X. Li, F. Gao, H.-O. Li, G. Xu, K. Wang, D. Liu, G. Cao, M. Xiao, T. Wang, J.-J. Zhang, G.-C. Guo, and G.-P. Guo, Coupling a Germanium Hut Wire Hole Quantum Dot to a Superconducting Microwave Resonator, *Nano Letters* **18**, 2091 (2018), pMID: 29468882.
- [75] A. Sammak, D. Sabbagh, N. W. Hendrickx, M. Lodari, B. Paquelet Wuetz, A. Tosato, L. Yeoh, M. Bollani, M. Virgilio, M. A. Schubert, P. Zaumseil, G. Capellini, M. Veldhorst, and G. Scappucci, Shallow and Undoped Germanium Quantum Wells: A Playground for Spin and Hybrid Quantum Technology, *Advanced Functional Materials* **29**, 1807613 (2019).
- [76] N. W. Hendrickx, W. I. Lawrie, M. Russ, F. van Riggelen, S. L. de Snoo, R. N. Schouten, A. Sammak, G. Scappucci, and M. Veldhorst, A four-qubit germanium quantum processor, *Nature* **591**, 580 (2021).
- [77] D. Jirovec, A. Hofmann, A. Ballabio, P. M. Mutter, G. Tavani, M. Botifoll, A. Crippa, J. Kukučka, O. Sagi, F. Martins, *et al.*, A singlet-triplet hole spin qubit in planar Ge, *Nature materials* **20**, 1106 (2021).
- [78] Z. Wang, E. Marcellina, A. R. Hamilton, J. H. Cullen, S. Rogge, J. Salfi, and D. Culcer, Optimal operation points for ultrafast, highly coherent Ge hole spin-orbit qubits, *npj Quantum Information* **7**, 54 (2021).
- [79] J. Xiang, A. Vidan, M. Tinkham, R. M. Westervelt, and C. M. Lieber, Ge/Si nanowire mesoscopic Josephson junctions, *Nature nanotechnology* **1**, 208 (2006).
- [80] N. Hendrickx, D. Franke, A. Sammak, M. Kouwenhoven, D. Sabbagh, L. Yeoh, R. Li, M. Tagliaferri, M. Virgilio, G. Capellini, *et al.*, Gate-controlled quantum dots and superconductivity in planar germanium, *Nature Communications* **9**, 2835 (2018).
- [81] J. Ridderbos, M. Brauns, J. Shen, F. K. de Vries, A. Li, E. P. Bakkers, A. Brinkman, and F. A. Zwanenburg, Josephson Effect in a Few-Hole Quantum Dot, *Advanced materials* **30**, 1802257 (2018).
- [82] N. W. Hendrickx, M. L. V. Tagliaferri, M. Kouwenhoven, R. Li, D. P. Franke, A. Sammak, A. Brinkman, G. Scappucci, and M. Veldhorst, Ballistic supercurrent discretization and micrometer-long Josephson coupling in germanium, *Phys. Rev. B* **99**, 075435 (2019).
- [83] F. Vigneau, R. Mizokuchi, D. C. Zanuz, X. Huang, S. Tan, R. Maurand, S. Frolov, A. Sammak, G. Scappucci, F. Lefloch, and S. De Franceschi, Germanium Quantum-Well Josephson Field-Effect Transistors and Interferometers, *Nano Letters* **19**, 1023 (2019).
- [84] K. Aggarwal, A. Hofmann, D. Jirovec, I. Prieto, A. Sammak, M. Botifoll, S. Martí-Sánchez, M. Veldhorst, J. Arbiol, G. Scappucci, J. Danon, and G. Katsaros, Enhancement of proximity-induced superconductivity in a planar Ge hole gas, *Phys. Rev. Res.* **3**, L022005 (2021).
- [85] A. Tosato, V. Levajac, J.-Y. Wang, C. J. Boor, F. Borsoi, M. Botifoll, C. N. Borja, S. Martí-Sánchez, J. Arbiol, A. Sammak, *et al.*, Hard superconducting gap in germanium, *Communications Materials* **4**, 23 (2023).
- [86] R. Moriya, K. Sawano, Y. Hoshi, S. Masubuchi, Y. Shiraki, A. Wild, C. Neumann, G. Abstreiter, D. Bougeard, T. Koga, and T. Machida, Cubic Rashba Spin-Orbit Interaction of a Two-Dimensional Hole Gas in a Strained-Ge/SiGe Quantum Well, *Phys. Rev. Lett.* **113**, 086601 (2014).
- [87] C. Morrison, P. Wiśniewski, S. Rhead, J. Foronda, D. Leadley, and M. Myronov, Observation of Rashba zero-field spin splitting in a strained germanium 2D hole gas, *Applied Physics Letters* **105**, 182401 (2014).
- [88] M. Failla, M. Myronov, C. Morrison, D. R. Leadley, and J. Lloyd-Hughes, Narrow heavy-hole cyclotron resonances split by the cubic rashba spin-orbit interaction in strained germanium quantum wells, *Phys. Rev. B* **92**, 045303 (2015).
- [89] R. Mizokuchi, P. Torresani, R. Maurand, Z. Zeng, Y.-M. Niquet, M. Myronov, and S. De Franceschi, Hole weak anti-localization in a strained-Ge surface quantum well, *Applied Physics Letters* **111**, 063102 (2017).
- [90] C.-T. Chou, N. T. Jacobson, J. E. Moussa, A. D. Baczewski, Y. Chuang, C.-Y. Liu, J.-Y. Li, and T. M. Lu, Weak anti-localization of two-dimensional holes in germanium beyond the diffusive regime, *Nanoscale* **10**, 20559 (2018).
- [91] X.-J. Hao, T. Tu, G. Cao, C. Zhou, H.-O. Li, G.-C. Guo, W. Y. Fung, Z. Ji, G.-P. Guo, and W. Lu, Strong and Tunable Spin-Orbit Coupling of One-Dimensional Holes in Ge/Si Core/Shell Nanowires, *Nano Letters* **10**, 2956 (2010).
- [92] N. Hendrickx, W. Lawrie, L. Petit, A. Sammak, G. Scappucci, and M. Veldhorst, A single-hole spin qubit, *Nature Communications* **11**, 3478 (2020).
- [93] N. Hendrickx, D. Franke, A. Sammak, G. Scappucci, and M. Veldhorst, Fast two-qubit logic with holes in germanium, *Nature* **577**, 487 (2020).
- [94] F. N. Froning, L. C. Camenzind, O. A. van der Molen, A. Li, E. P. Bakkers, D. M. Zumbühl, and F. R. Braakman, Ultrafast hole spin qubit with gate-tunable spin-

- orbit switch functionality, *Nature Nanotechnology* **16**, 308 (2021).
- [95] S. Bosco, M. Benito, C. Adelsberger, and D. Loss, Squeezed hole spin qubits in ge quantum dots with ultrafast gates at low power, *Phys. Rev. B* **104**, 115425 (2021).
- [96] K. Wang, G. Xu, F. Gao, H. Liu, R.-L. Ma, X. Zhang, Z. Wang, G. Cao, T. Wang, J.-J. Zhang, D. Culcer, X. Hu, H.-W. Jiang, H.-O. Li, G.-C. Guo, and G.-P. Guo, Ultrafast coherent control of a hole spin qubit in a germanium quantum dot, *Nature Communications* **13**, 206 (2022).
- [97] E. Marcellina, A. R. Hamilton, R. Winkler, and D. Culcer, Spin-orbit interactions in inversion-asymmetric two-dimensional hole systems: A variational analysis, *Phys. Rev. B* **95**, 075305 (2017).
- [98] L. A. Terrazos, E. Marcellina, Z. Wang, S. N. Copper-smith, M. Friesen, A. R. Hamilton, X. Hu, B. Koiller, A. L. Saraiva, D. Culcer, and R. B. Capaz, Theory of hole-spin qubits in strained germanium quantum dots, *Phys. Rev. B* **103**, 125201 (2021).
- [99] V. P. Michal, B. Venitucci, and Y.-M. Niquet, Longitudinal and transverse electric field manipulation of hole spin-orbit qubits in one-dimensional channels, *Phys. Rev. B* **103**, 045305 (2021).
- [100] Furthermore, metalization of a semiconductor by a superconductor usually decreases the SOI [33, 34]; however, it was recently shown that metalization also modifies the wave functions in Ge such that the SOI can actually increase [130].
- [101] H. Watzinger, C. Kloeffel, L. Vukušić, M. D. Rossell, V. Sessi, J. Kukučka, R. Kirchschrager, E. Lausecker, A. Truhlar, M. Glaser, A. Rastelli, A. Fuhrer, D. Loss, and G. Katsaros, Heavy-Hole States in Germanium Hut Wires, *Nano Letters* **16**, 6879 (2016).
- [102] T. Lu, C. Harris, S.-H. Huang, Y. Chuang, J.-Y. Li, and C. Liu, Effective g factor of low-density two-dimensional holes in a Ge quantum well, *Applied Physics Letters* **111**, 102108 (2017).
- [103] A. Hofmann, D. Jirovec, M. Borovkov, I. Prieto, A. Balabio, J. Frigerio, D. Chrastina, G. Isella, and G. Katsaros, Assessing the potential of Ge/SiGe quantum dots as hosts for singlet-triplet qubits, arXiv:1910.05841 (2019).
- [104] F. Gao, J.-H. Wang, H. Watzinger, H. Hu, M. J. Rančić, J.-Y. Zhang, T. Wang, Y. Yao, G.-L. Wang, J. Kukučka, *et al.*, Site-controlled uniform Ge/Si hut wires with electrically tunable spin-orbit coupling, *Advanced Materials* **32**, 1906523 (2020).
- [105] F. Maier, J. Klinovaja, and D. Loss, Majorana fermions in ge/si hole nanowires, *Phys. Rev. B* **90**, 195421 (2014).
- [106] M. Luethi, K. Laubscher, S. Bosco, D. Loss, and J. Klinovaja, Planar Josephson junctions in germanium: Effect of cubic spin-orbit interaction, *Phys. Rev. B* **107**, 035435 (2023).
- [107] F. Zhang, C. L. Kane, and E. J. Mele, Time-Reversal-Invariant Topological Superconductivity and Majorana Kramers Pairs, *Phys. Rev. Lett.* **111**, 056402 (2013).
- [108] S. Nakosai, J. C. Budich, Y. Tanaka, B. Trauzettel, and N. Nagaosa, Majorana Bound States and Nonlocal Spin Correlations in a Quantum Wire on an Unconventional Superconductor, *Phys. Rev. Lett.* **110**, 117002 (2013).
- [109] A. Keselman, L. Fu, A. Stern, and E. Berg, Inducing Time-Reversal-Invariant Topological Superconductivity and Fermion Parity Pumping in Quantum Wires, *Phys. Rev. Lett.* **111**, 116402 (2013).
- [110] J. Klinovaja and D. Loss, Time-reversal invariant parafermions in interacting Rashba nanowires, *Phys. Rev. B* **90**, 045118 (2014).
- [111] A. Haim, A. Keselman, E. Berg, and Y. Oreg, Time-reversal-invariant topological superconductivity induced by repulsive interactions in quantum wires, *Phys. Rev. B* **89**, 220504 (2014).
- [112] E. Gaidamauskas, J. Paaske, and K. Flensberg, Majorana Bound States in Two-Channel Time-Reversal-Symmetric Nanowire Systems, *Phys. Rev. Lett.* **112**, 126402 (2014).
- [113] E. Dumitrescu, J. D. Sau, and S. Tewari, Magnetic field response and chiral symmetry of time-reversal-invariant topological superconductors, *Phys. Rev. B* **90**, 245438 (2014).
- [114] A. Haim, K. Wölms, E. Berg, Y. Oreg, and K. Flensberg, Interaction-driven topological superconductivity in one dimension, *Phys. Rev. B* **94**, 115124 (2016).
- [115] C. Schrade, M. Thakurathi, C. Reeg, S. Hoffman, J. Klinovaja, and D. Loss, Low-field topological threshold in Majorana double nanowires, *Phys. Rev. B* **96**, 035306 (2017).
- [116] M. Thakurathi, P. Simon, I. Mandal, J. Klinovaja, and D. Loss, Majorana Kramers pairs in Rashba double nanowires with interactions and disorder, *Phys. Rev. B* **97**, 045415 (2018).
- [117] A. A. Aligia and L. Arrachea, Entangled end states with fractionalized spin projection in a time-reversal-invariant topological superconducting wire, *Phys. Rev. B* **98**, 174507 (2018).
- [118] F. Setiawan, A. Stern, and E. Berg, Topological superconductivity in planar Josephson junctions: Narrowing down to the nanowire limit, *Phys. Rev. B* **99**, 220506 (2019).
- [119] B. Scharf, F. Pientka, H. Ren, A. Yacoby, and E. M. Hankiewicz, Tuning topological superconductivity in phase-controlled Josephson junctions with Rashba and Dresselhaus spin-orbit coupling, *Phys. Rev. B* **99**, 214503 (2019).
- [120] O. Dmytruk, M. Thakurathi, D. Loss, and J. Klinovaja, Majorana bound states in double nanowires with reduced Zeeman thresholds due to supercurrents, *Phys. Rev. B* **99**, 245416 (2019).
- [121] A. Cook and M. Franz, Majorana fermions in a topological-insulator nanowire proximity-coupled to an s-wave superconductor, *Phys. Rev. B* **84**, 201105 (2011).
- [122] S. Vaitiekėnas, G. W. Winkler, B. van Heck, T. Karzig, M.-T. Deng, K. Flensberg, L. I. Glazman, C. Nayak, P. Krogstrup, R. M. Lutchyn, and C. M. Marcus, Flux-induced topological superconductivity in full-shell nanowires, *Science* **367**, eaav3392 (2020).
- [123] H. F. Legg, D. Loss, and J. Klinovaja, Majorana bound states in topological insulators without a vortex, *Phys. Rev. B* **104**, 165405 (2021).
- [124] O. Lesser, Y. Oreg, and A. Stern, One-dimensional topological superconductivity based entirely on phase control, *Phys. Rev. B* **106**, L241405 (2022).
- [125] R. Winkler, *Spin-Orbit Coupling Effects in Two-Dimensional Electron and Hole Systems* (Springer-Verlag, Berlin, Heidelberg, New York, 2003).
- [126] Although it is possible for systems with only linear (Rashba) SOI to have different Fermi velocities, e.g. due

- to momentum dependence of the mass, the low filling of semiconductors means that such effects are typically weak.
- [127] R. M. A. Dantas, H. F. Legg, S. Bosco, D. Loss, and J. Klinovaja, Determination of spin-orbit interaction in semiconductor nanostructures via nonlinear transport, *Phys. Rev. B* **107**, L241202 (2023).
- [128] J. Klinovaja and D. Loss, Composite Majorana fermion wave functions in nanowires, *Phys. Rev. B* **86**, 085408 (2012).
- [129] C. W. J. Beenakker, Universal limit of critical-current fluctuations in mesoscopic Josephson junctions, *Phys. Rev. Lett.* **67**, 3836 (1991).
- [130] C. Adelsberger, H. F. Legg, D. Loss, and J. Klinovaja, Microscopic analysis of proximity-induced superconductivity and metallization effects in superconductor-germanium hole nanowires, *Phys. Rev. B* **108**, 155433 (2023).